

An Overview on Over-the-air Electromagnetic Signal Processing

Davide Dardari, *Fellow, IEEE*,

Giulia Torcolacci, *Graduate Student Member, IEEE*,

Gianni Pasolini, *Member, IEEE*, and Nicolò Decarli, *Member, IEEE*

Abstract

This article provides a tutorial on *over-the-air electromagnetic signal processing (ESP)* for next-generation wireless networks, addressing the limitations of digital processing to enhance the efficiency and sustainability of future 6th Generation (6G) systems. It explores the integration of electromagnetism and signal processing (SP) highlighting how their convergence can drive innovations for 6G technologies. Key topics include electromagnetic (EM) wave-based processing, the application of metamaterials and advanced antennas to optimize EM field manipulation with a reduced number of radiofrequency chains, and their applications in holographic multiple-input multiple-output systems. By showcasing enabling technologies and use cases, the article demonstrates how wave-based processing can minimize energy consumption, complexity, and latency, offering an effective framework for more sustainable and efficient wireless systems. This article aims to assist researchers and professionals in integrating advanced EM technologies with conventional SP methods.

arXiv:2412.14968v2 [eess.SP] 20 Dec 2024

I. INTRODUCTION

AFTER the publication of Shannon's landmark paper in 1948, the digital revolution rapidly accelerated, shifting information processing and communication from the analog realm to the digital domain. The exponential growth in digital computing capabilities has pushed the boundary between analog and digital processing in wireless systems closer to the devices' antennas. This transition is mainly driven by software-defined radio implementations, which have shifted most analog processing to radio-frequency (RF) circuits, primarily utilizing guided wave electromagnetic (EM) structures. Except for optical systems, where analog computing has been established for several years and remains an active research area [1], most signal processing in wireless systems occurs in the digital domain at baseband. In these systems, RF circuits are primarily responsible for basic operations such as up-down conversion, phase shifts, and amplification. However, this approach could be questioned when addressing the design of next-generation wireless systems, such as 6th Generation (6G) networks, which are expected to impose extremely stringent requirements to offer enhanced performance in terms of capacity, reliability, reduced latency, and new functionalities like integrated sensing and communications (ISAC) [2], [3]. So far, these needs have been addressed using various solutions, such as small cells, millimeter wave (mmWave) communications, and massive multiple-input multiple-output (MIMO) systems, which have demonstrated their ability to improve network capacity and provide ubiquitous connectivity [4].

Nonetheless, these well-established technologies and design practices no longer appear sufficient to achieve the performance levels required for future wireless networks. In fact, the evolution towards 6G is driving the exploration of the fundamental limits of wireless communication and innovative design paradigms to meet the stringent requirements posed by next-generation networks [4], [5]. For instance, the use of higher frequency bands, e.g., terahertz (THz), and electrically large antenna arrays, e.g., based on metasurfaces and extremely large-scale multiple-input multiple-output (XL-MIMO) configurations, are key enablers of this evolution [6]. Interestingly, their joint utilization enables the system's operation in the radiative near-field region of the antennas, thus leading to unprecedented levels of communication and sensing performance, flexibility, and resolution [7], [8]. However, we have reached the point where further advancing the capabilities of already established technologies and incorporating new ones is hindered by issues related to practical implementation, hardware cost, and complexity, as well as excessive processing time and power consumption. These issues often result in the so-called "digital bottleneck", posing a substantial challenge to the feasibility, scalability, and sustainability of future wireless networks.

Therefore, it is increasingly evident that it is necessary to reverse the current trend and conceive solutions where at least part of the signal processing occurs in the analog domain at RF. For instance,

hybrid digital-analog solutions in MIMO systems have been extensively explored to mitigate digital processing burdens, though often at the cost of reduced flexibility [4]. Nevertheless, current hybrid solutions are not sufficient and radically new physical layer technologies, featuring a more balanced integration between digital and analog RF processing, have to be found.

A promising approach toward this goal is to transfer part of the signals' processing directly to the EM level [9]–[14]. This approach is known as *over-the-air electromagnetic signal processing (ESP)*, also referred to as *electromagnetic signal and information theory (ESIT)* or *electromagnetic information theory (EIT)*. Specifically, ESP can be defined as an interdisciplinary scientific field focused on exploiting the synergies between innovative EM technologies, signal processing (SP) algorithms, and information theory. This term refers to the study and development of novel technological solutions where an EM wave generated by one or more radiating sources is perturbed during propagation, i.e., over the air, by reconfigurable EM structures. This approach aims to achieve specific SP functions with lower energy consumption, complexity, and latency (the processing takes place at the speed of light) compared to their digital counterparts. In addition, ESP can be considered as part of the more general *holographic communications* framework, which is envisioned as a holistic way to manipulate the EM field generated or sensed by the antennas with unprecedented flexibility [8]. This paradigm involves designing reconfigurable radio propagation environments [15] that can arbitrarily control signal transmission, manipulation, and reflection through the massive deployment of peculiar EM devices based on metamaterials. In these devices, the reflection, refraction, or scattering properties of a set of reconfigurable scatterers composing their structure are optimized to achieve specific processing and radiation characteristics.

Admittedly, many of the studies on the design of innovative EM structures and processing algorithms are still in their infancy, and significant progress is needed in terms of practical implementations and concrete applications. The seamless integration of electromagnetism and SP offers a transformative opportunity for advancing next-generation wireless networks, particularly through the emergence of ESP. As we progress towards 6G systems, the SP community encounters new challenges that require a reassessment of traditional methods and a shift towards innovative approaches.

The primary objective of this article is to present in a unified way the fundamental limits and the new opportunities in processing EM waves using physically consistent models. While traditional SP techniques are effective in the digital realm, they often struggle with the complexities and constraints posed by EM environments and emerging EM technologies. This discrepancy underscores the necessity for specialized SP algorithms that align with the physical properties and constraints of EM waves. This article seeks to shed light on this issue and wants to provide a survey of recent advancements in ESP. It emphasizes the importance of bridging EM theory with SP and advocates for a unified strategy to enhance the sustainability of wireless communication technologies. Targeted at

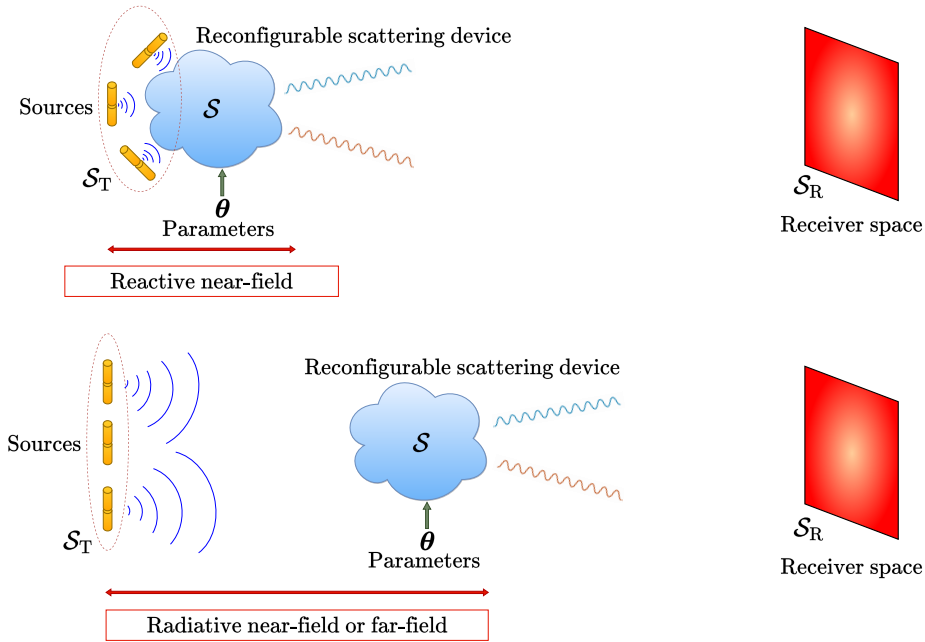


Fig. 1. EM signal processing performed in the reactive near field (top) or in the radiative near field (or far-field) (bottom) regions of the sources using a reconfigurable scattering device.

readers with expertise in SP and/or wireless communications, the article begins with a brief historical overview before revisiting fundamental EM principles needed to establish a general framework for exploring the fundamental limits and practical algorithms of ESP. Key technologies will be presented as specific cases, supported by numerical examples that underscore the need for electromagnetically consistent optimization algorithms. By addressing the limitations, opportunities, and challenges of this integrated ESP approach, we aim to inspire further research and provide valuable insights. We hope this work serves as a useful resource for researchers and practitioners, highlighting the essential role of integrating these disciplines in driving innovative solutions and applications for future 6G networks.

II. “OVER-THE-AIR” EM-BASED SIGNAL PROCESSING: AN OLD IDEA MADE NEW

In a general setting, ESP refers to the capability of processing EM waves over the air by introducing one or more reconfigurable scattering devices between the source and receiver spaces, denoted as S_T and S_R , respectively (see Fig. 1). Typically, these reconfigurable scattering devices are linear and passive structures thus reducing their power consumption close to zero. Let S denote the space occupied by the scattering device. The configuration of the device can be modified using a set of parameters, θ , which vary depending on the specific implementation technology. The scenario shown in Fig. 1 can encompass various ESP technologies and geometric configurations. Specifically, ESP solutions can generally be categorized into two types:

- *Reactive region configuration*: The scattering device is located in the reactive region of the source space so that inductive coupling takes place between them (see Fig. 1, top). Its role includes enabling large antenna arrays while minimizing the number of RF chains, reducing power consumption, and lowering latency compared to traditional solutions. Additionally, it can support the implementation of complex functionalities in the analog domain. The dual scheme where the scattering device is located close to the receiver space is also possible.
- *Radiative near and far field region configuration*: The reconfigurable scattering device is positioned in the radiative region of the source and receiver spaces and it is used to control the propagation environment. This approach offers a cost-effective alternative to deploying additional access points (see Fig. 1, bottom). In some configurations, the source and receiver spaces might match (see Sec.V-C).

Regardless of the category above or specific technology, the core ESP problem can be formulated as follows. Given a set of sources located in the source space \mathcal{S}_T , determine the configuration θ of the scattering device that generates the desired EM field at the receiver space \mathcal{S}_R , while satisfying the constraints imposed by EM laws and the selected technology. A further step involves making the set of parameters θ dependent on data generated within the scattering device itself (e.g., by a sensor in an Internet of things (IoT) application). This allows the information to be directly embedded into the reflected signal, removing the need for additional RF signal generation. Consequently, this approach can significantly reduce energy consumption at the sensor side [16]–[18].

Notably, the concept of reconfigurable scatterers has a long and well-established history in the field of antenna theory. A pivotal milestone and precursor to contemporary solutions is R. Harrington's theory of loaded scatterers, which is closely associated with characteristic mode decomposition. This theory involves configuring scatterers such that the principal radiating mode of the EM structure, when illuminated by the source wave, aligns with the desired response [19]. This theory was later extended, also by R. Harrington, to reactively controlled arrays. In this context, passive scattering elements are positioned near a radiating antenna to exploit mutual coupling within the reactive near-field region, thereby modifying the antenna's radiation characteristics [20].

In recent years, these concepts have been revisited and advanced thanks to technological and material innovations, enabling the development of new EM structures that address the increasing demand for enhanced performance, flexibility, and cost efficiency in future wireless systems. A notable example is given by metasurfaces, which are bi-dimensional (2D) structures, either homogeneous or inhomogeneous, composed of interacting sub-wavelength-sized cells called meta-atoms. These structures may provide control of the reflected and transmitted EM field [21], [22]. Both metasurfaces and more conventional solutions, such as backscattering antenna arrays, have facilitated the development of reconfigurable intelligent surfaces (RISs), which have garnered significant interest within the scientific

community. RISs are primarily used to manipulate the propagation environment and are considered a cornerstone of the emerging *smart radio environments* paradigm, whose aim is to integrate the propagation environment into the system's design and optimization loop [23], [24]. Specifically, RISs belong to the second category, shown in Fig. 1 (bottom), where they are typically employed to control the propagation environment [24], [25].

Within the first category shown in Fig. 1 (top), there is a wide variety of promising technologies. These include XL-MIMO arrays (also known as extremely large antenna arrays (ELAAs)) [26], large intelligent surfaces (LISs) or holographic multiple-input multiple-output (HMIMO) surfaces [5], [27], dynamic metasurface antennas (DMAs) [7], fluid and reconfigurable antennas [28], and the latest developments in reactively controlled arrays, such as electrically steerable passive array radiators (ESPARs) and dynamic scattering arrays (DSAs) [29], [30]. Significant advancements have concurrently been made in the optical community with the development of all-optical diffractive deep neural networks (DNNs) [31], and a similar concept has recently been applied to RF systems [32], inspiring the development of the stacked intelligent metasurface (SIM) technology, even though this technology is currently limited to linear processing capabilities [33]. Additionally, the introduction of novel volumetric metamaterials has enabled three-dimensional (3D) EM processing functions, such as first-derivative computation [34].

As discussed in the following sections, a key feature of novel EM structures from an SP perspective is their ability to perform complex operations at the EM level. Some of the processing functions that can be achieved include over-the-air computation of the singular value decomposition (SVD) of the MIMO channel matrix, spatial derivatives, MIMO EM precoding, and direction-of-arrival (DoA) signal estimation.

III. A GENERAL FRAMEWORK FOR EM SIGNAL PROCESSING

This section presents a unified conceptual framework for ESP, treating the EM processing structure as a feedback space-variant linear system and relating it to modal analysis. This approach creates a connection between EM theory and SP, outlining the theoretical foundations and performance limits concerning potential processing flexibility.

A. Preliminaries: The Green Operator and the Wavenumber Representation

We consider a generic space \mathcal{S}_T characterized by the monochromatic current density $\mathbf{J}(\mathbf{r})$ in A/m^2 , with $\mathbf{r} = r_x\hat{\mathbf{x}} + r_y\hat{\mathbf{y}} + r_z\hat{\mathbf{z}} \in \mathcal{S}_T$ being the position vector and $\hat{\mathbf{x}}$, $\hat{\mathbf{y}}$, and $\hat{\mathbf{z}}$ the 3D unit vectors. The time dependence $e^{j\omega t}$, with ω being the angular frequency, has been omitted. In general, space \mathcal{S}_T is a volume, but it may also represent a surface or a wire source. The current density $\mathbf{J}(\mathbf{r})$ can be an impressed current in the case of an active source, such as a transmitting antenna, or an

induced/equivalent current in the case of a scattering device. The electrical field $\mathbf{E}(\mathbf{r})$ [V/m] generated by $\mathbf{J}(\mathbf{r})$ can be computed under the free-space condition by considering the Helmholtz equation, whose solution is given by [35]

$$\mathbf{E}(\mathbf{r}) = \int_{\mathcal{S}_T} \mathbf{G}(\mathbf{r} - \mathbf{s}) \mathbf{J}(\mathbf{s}) d\mathbf{s} = (\mathbb{G}\mathbf{J})(\mathbf{r}). \quad (1)$$

Equation (1) implicitly defines the Green's tensor operator \mathbb{G} , with $\mathbf{G}(\mathbf{r})$ being the dyadic Green function defined as [35]

$$\mathbf{G}(\mathbf{r}) = -j \frac{\eta e^{-jk_0|\mathbf{r}|}}{2\lambda|\mathbf{r}|} \cdot \left[\left(\mathbf{I} - \hat{\mathbf{r}}\hat{\mathbf{r}}^T \right) + \frac{j\lambda}{2\pi|\mathbf{r}|} \left(\mathbf{I} - 3\hat{\mathbf{r}}\hat{\mathbf{r}}^T \right) - \frac{\lambda^2}{(2\pi|\mathbf{r}|)^2} \left(\mathbf{I} - 3\hat{\mathbf{r}}\hat{\mathbf{r}}^T \right) \right] \quad (2)$$

where $k_0 = 2\pi/\lambda$ is the wavenumber, λ is the wavelength, $\hat{\mathbf{r}} = \mathbf{r}/|\mathbf{r}|$, and η is the free-space impedance. $\mathbf{G}(\mathbf{r})$ is the solution of the Helmholtz equation for an impulsive current density $\mathbf{J}(\mathbf{r}) = \mathbf{l} \cdot \delta(\mathbf{r})$, with \mathbf{l} being the unit dyadic,¹ and $\delta(\mathbf{r})$ the delta Dirac pseudo-function. When $|\mathbf{r}| \gg \lambda$, only the first term in (2) contributes to the EM radiation. The electrical field in the current-free portion of the space must satisfy the homogeneous wave equation [35]

$$\nabla^2 \mathbf{E}(\mathbf{r}) + k_0^2 \mathbf{E}(\mathbf{r}) = 0 \quad (3)$$

where ∇^2 represents the Laplacian operator.

For what follows, it is convenient to introduce the representation of the fields in the wavenumber domain $\boldsymbol{\kappa} = \kappa_x \hat{\mathbf{x}} + \kappa_y \hat{\mathbf{y}} + \kappa_z \hat{\mathbf{z}}$ through the 3D Fourier transform. Specifically, given a generic field $\mathbf{A}(\mathbf{r})$, we define

$$\tilde{\mathbf{A}}(\boldsymbol{\kappa}) = \mathcal{F}_3[\mathbf{A}(\mathbf{r})] = \int_{\mathbb{R}^3} \mathbf{A}(\mathbf{r}) e^{-j\boldsymbol{\kappa} \cdot \mathbf{r}} d\mathbf{r} \quad (4)$$

with \cdot denoting the scalar product.

By applying the Fourier transform to both sides of (3) we obtain

$$\left(\kappa_x^2 + \kappa_y^2 + \kappa_z^2 - k_0^2 \right) \tilde{\mathbf{E}}(\boldsymbol{\kappa}) = 0 \quad (5)$$

where we have considered that $\mathcal{F}_3[\nabla^2 \mathbf{A}(\mathbf{r})] = -|\boldsymbol{\kappa}|^2 \tilde{\mathbf{A}}(\boldsymbol{\kappa})$. The structure of (5) implies that $\tilde{\mathbf{E}}(\boldsymbol{\kappa}) = \mathcal{F}_3[\mathbf{E}(\mathbf{r})]$ must vanish everywhere except on the wavenumber support

$$\mathcal{E} = \{ (\kappa_x, \kappa_y, \kappa_z) \in \mathbb{R}^3 : \kappa_x^2 + \kappa_y^2 + \kappa_z^2 = k_0^2 \}. \quad (6)$$

In other words, the EM propagation phenomenon acts as a filter in the wavenumber domain with support in \mathcal{E} . Since $\tilde{\mathbf{E}}(\boldsymbol{\kappa})$ is defined over a support with zero measure in the waveform domain, it is not an ordinary function but takes the form [36]

$$\tilde{\mathbf{E}}(\boldsymbol{\kappa}) = \tilde{\mathbf{E}}_0(\boldsymbol{\kappa}) \delta \left(\kappa_x^2 + \kappa_y^2 + \kappa_z^2 - k_0^2 \right) \quad (7)$$

¹The unit dyadic, also known as the identity dyadic or unit tensor, is a mathematical construct in vector and tensor analysis. It is the second-order tensor equivalent of the scalar number 1 in scalar algebra or the identity matrix in linear algebra.

where $\tilde{\mathbf{E}}_0(\boldsymbol{\kappa})$ defines the angular dependence (direction) of the wave. When applied to the EM field $\mathbf{E}(\mathbf{r})$ in the presence of current sources, the inverse Fourier representation expresses it in terms of mathematical plane waves [15], [37]

$$\begin{aligned} \mathbf{E}(\mathbf{r}) &= \mathcal{F}_3^{-1} [\tilde{\mathbf{E}}(\boldsymbol{\kappa})] = \frac{1}{(2\pi)^3} \int_{\mathbb{R}^3} \tilde{\mathbf{E}}(\boldsymbol{\kappa}) e^{j\boldsymbol{\kappa}\cdot\mathbf{r}} d\boldsymbol{\kappa} = \frac{1}{(2\pi)^3} \int_{\mathbb{R}^3} \tilde{\mathbf{G}}(\boldsymbol{\kappa}) \tilde{\mathbf{J}}(\boldsymbol{\kappa}) e^{j\boldsymbol{\kappa}\cdot\mathbf{r}} d\boldsymbol{\kappa} \\ &= \frac{j\eta}{k_0(2\pi)^3} \int_{\mathbb{R}^3} \frac{\boldsymbol{\kappa} \times \boldsymbol{\kappa} \times \tilde{\mathbf{J}}(\boldsymbol{\kappa})}{|\boldsymbol{\kappa}|^2 - k_0^2} e^{j\boldsymbol{\kappa}\cdot\mathbf{r}} d\boldsymbol{\kappa} \end{aligned} \quad (8)$$

where $\tilde{\mathbf{G}}(\boldsymbol{\kappa}) = \mathcal{F}_3 [\mathbf{G}(\mathbf{r})]$, $\tilde{\mathbf{J}}(\boldsymbol{\kappa}) = \mathcal{F}_3 [\mathbf{J}(\mathbf{r})]$, and \times denotes the cross product. In fact, for a fixed wavenumber $\boldsymbol{\kappa}$, $\tilde{\mathbf{E}}(\boldsymbol{\kappa}) e^{j\boldsymbol{\kappa}\cdot\mathbf{r}}$ in (8) represents a plane wave with “direction” $\boldsymbol{\kappa}/k_0$. It is interesting to emphasize that the generic plane wave $\tilde{\mathbf{E}}(\boldsymbol{\kappa}) e^{j\boldsymbol{\kappa}\cdot\mathbf{r}} = \tilde{\mathbf{E}}(\boldsymbol{\kappa}) e^{j\kappa_x r_x} e^{j\kappa_y r_y} e^{j\kappa_z r_z}$ in (8) radiates $\forall \mathbf{r}$, i.e., in all the 3D space, only when κ_x , κ_y , and κ_z are all real (*visible region*). Vice versa, if at least one of them is complex,² let us say κ_z , it is $e^{j\kappa_z r_z} = e^{-|\kappa_z r_z|} \rightarrow 0$ for $|r_z|$ larger than a few wavelengths and the wave becomes evanescent, i.e., it does not radiate (*invisible region*). In summary, only the spectral components of $\tilde{\mathbf{E}}(\boldsymbol{\kappa})$ for $\boldsymbol{\kappa} \in \mathcal{E}$ represent EM waves, i.e., are physically consistent, and only the subset having real components radiates. For each wavenumber, i.e., plane wave, because of the $\boldsymbol{\kappa} \times \boldsymbol{\kappa} \times \tilde{\mathbf{J}}(\boldsymbol{\kappa})$ term in (8), $\tilde{\mathbf{E}}(\boldsymbol{\kappa})$ is subject to the relation $\tilde{\mathbf{E}}(\boldsymbol{\kappa}) \cdot \boldsymbol{\kappa} = 0$, limiting to two the degrees-of-freedom (DoF) achievable with different polarizations [37]. Incidentally, for locations \mathbf{r} in the far-field region of the source, (8) can be approximated as [35, Ch. 12]

$$\mathbf{E}(\mathbf{r}) \simeq j k_0 \eta \frac{e^{-j k_0 |\mathbf{r}|}}{4\pi |\mathbf{r}|} \hat{\mathbf{r}} \times \hat{\mathbf{r}} \times \tilde{\mathbf{J}}(k_0 \hat{\mathbf{r}}) \quad (9)$$

so that the EM field becomes directly related to the Fourier transform of the source evaluated at direction $k_0 \hat{\mathbf{r}} \in \mathcal{E}$.

B. Communication Modes

For convenience, we introduce the inner product between vector functions $\mathbf{A}(\mathbf{r})$ and $\mathbf{B}(\mathbf{r})$, defined on the generic space \mathcal{S} , as

$$\langle \mathbf{A}(\mathbf{r}), \mathbf{B}(\mathbf{r}) \rangle = \int_{\mathcal{S}} \mathbf{A}(\mathbf{r}) \cdot \mathbf{B}^*(\mathbf{r}) d\mathbf{r}. \quad (10)$$

Two vector functions are said to be orthogonal if $\langle \mathbf{A}(\mathbf{r}), \mathbf{B}(\mathbf{r}) \rangle = 0$.

A fundamental question is determining how many orthogonal communication channels—referred to as *communication modes*—can be exploited between a source space \mathcal{S}_T and a receiver space \mathcal{S}_R while maximizing the coupling intensity (see Fig. 2). This is associated with the optimal approximation of every element in the image space of a Hilbert-Schmidt operator in terms of singular functions.

²For example, this might happen if $\kappa_x^2 + \kappa_y^2 > k_0^2$ so that to satisfy (6) it should be $\kappa_z = j\sqrt{\kappa_x^2 + \kappa_y^2 - k_0^2} \in \mathbb{C}$.

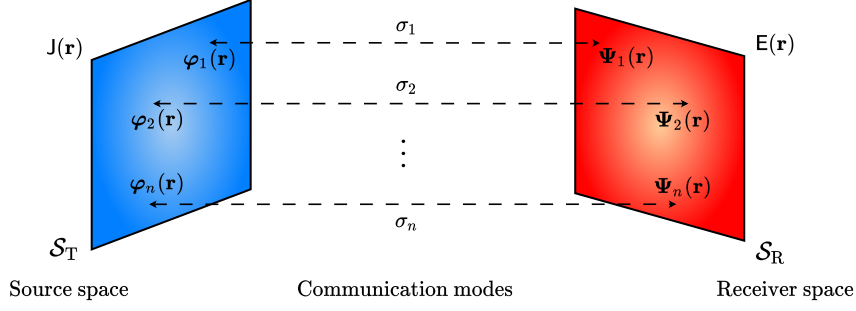


Fig. 2. Communication modes between two spaces.

Specifically, define $\mathcal{X} = \mathbb{L}^2(\mathcal{S}_T)$ and $\mathcal{Y} = \mathbb{L}^2(\mathcal{S}_R)$ the Hilbert spaces corresponding to the square-integrable functions defined in \mathcal{S}_T and \mathcal{S}_R , respectively. The function $\mathbf{E}(\mathbf{r}) \in \mathcal{Y}$ can be seen as the image of $\mathbf{J}(\mathbf{r}) \in \mathcal{X}$ through the Hilbert-Schmidt kernel $\mathbb{G}(\mathbf{r}, \mathbf{s}) = \mathbb{G}(\mathbf{r} - \mathbf{s})$ on $\mathcal{S}_T \times \mathcal{S}_R$, which induces the operator $\mathbb{G} : \mathcal{X} \rightarrow \mathcal{Y}$ such that, for any $\mathbf{J}(\mathbf{r}) \in \mathcal{X}$, we can write (1). Define the following self-adjoint Hilbert-Schmidt operators $\mathbb{G}\mathbb{G}^*$ and $\mathbb{G}^*\mathbb{G}$ and let $\{\varphi_n(\mathbf{r})\}$ and $\{\Psi_n(\mathbf{r})\}$ be the eigenfunctions, associated with eigenvalues σ_n^2 , of the following coupled eigenfunction problems [38]

$$(\mathbb{G}\mathbb{G}^* \varphi_n)(\mathbf{r}) = \sigma_n^2 \varphi_n(\mathbf{r}) \quad (\mathbb{G}^*\mathbb{G} \Psi_n)(\mathbf{r}) = \sigma_n^2 \Psi_n(\mathbf{r}). \quad (11)$$

An important property of Hilbert-Schmidt operators is that they are compact and admit either a finite or countably infinite orthonormal basis. In particular, two sets of orthonormal eigenfunctions $\{\varphi_n(\mathbf{r})\}$, $\{\Psi_n(\mathbf{r})\}$ exist, which are solutions, respectively, of the coupled eigenfunction problems in (11) with the same real eigenvalues $\sigma_1^2 \geq \sigma_2^2 \geq \sigma_3^2 \dots$ [38], [39]. Note that $\{\varphi_n(\mathbf{r})\}$ and $\{\Psi_n(\mathbf{r})\}$ are two sets of orthonormal (vector) functions that are complete, respectively, in \mathcal{S}_T and \mathcal{S}_R . The orthonormal condition implies that $\langle \varphi_k(\mathbf{r}), \varphi_n(\mathbf{r}) \rangle = \delta_{k-n}$, and similarly, the same condition holds for the set $\{\Psi_n(\mathbf{r})\}$. In general, the eigenvalues have significant magnitudes up to a certain value σ_N^2 , i.e., the sum of the σ_n^2 's for $n > N$ is negligible with respect to the sum of the first N eigenvalues, so that we can consider up to N well-coupled communication modes between the two spaces. The number N is often called the number of DoF available in the link. Detailed discussion on optimal approximation and the definition of DoF can be found in [38].

In summary, the finite coupling operator \mathbb{G} between finite spaces \mathcal{S}_T and \mathcal{S}_R is a Hilbert-Schmidt operator, and up to N communication modes (i.e., orthogonal channels) can be identified for a given level of approximation accuracy, each of them represented by the triad $(\varphi_n(\mathbf{r}), \Psi_n(\mathbf{r}), \sigma_n)$. It follows that the current density $\mathbf{J}(\mathbf{r})$ on the space \mathcal{S}_T , i.e., for $\mathbf{r} \in \mathcal{S}_T$, can be well approximated as a linear combination of the basis functions

$$\mathbf{J}(\mathbf{r}) \simeq \sum_{n=1}^N j_n \varphi_n(\mathbf{r}) \quad (12)$$

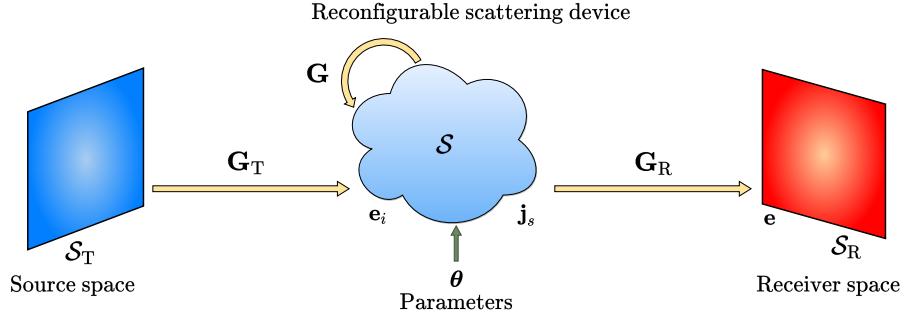


Fig. 3. A source and receiver space interacting through a reconfigurable scattering device.

where the complex coefficients j_n are given by $j_n = \langle \mathbf{J}(\mathbf{r}), \varphi_n(\mathbf{r}) \rangle$, for $n = 1, 2, \dots, N$. Similarly, it holds for $\mathbf{E}(\mathbf{r})$ in \mathcal{S}_R through the basis set $\{\Psi_n(\mathbf{r})\}$

$$\mathbf{E}(\mathbf{r}) \simeq \sum_{n=1}^N e_n \Psi_n(\mathbf{r}) = \sum_{n=1}^N \sigma_n j_n \Psi_n(\mathbf{r}). \quad (13)$$

C. Reconfigurable Scattering Device: Mode Transfer Matrix

Consider now the scenario illustrated in Fig. 3, where a source space \mathcal{S}_T (e.g., a transmitter) and a receiver space \mathcal{S}_R (the receiver) interact through a reconfigurable scattering device. We consider the reconfigurable scattering device to be enclosed within the finite space \mathcal{S} . The impinging EM field generated by currents located in the source space \mathcal{S}_T induces a current distribution $\mathbf{J}_s(\mathbf{r})$ on the scattering device, with $\mathbf{r} \in \mathcal{S}$, that radiates the scattered field $\mathbf{E}_s(\mathbf{r})$ [35].³

For any linear time-invariant scattering object, the induced current density $\mathbf{J}_s(\mathbf{r})$, $\mathbf{r} \in \mathcal{S}$, is a linear functional of the EM field $\mathbf{E}(\mathbf{r})$ that can be described as

$$\mathbf{J}_s(\mathbf{r}) = \int_{\mathcal{S}} \mathbf{D}(\mathbf{r}, \mathbf{s}) \mathbf{E}(\mathbf{s}) d\mathbf{s} = (\mathbb{D} \mathbf{E})(\mathbf{r}) \quad (14)$$

where $\mathbf{D}(\mathbf{r}, \mathbf{s})$ is the impulse response dyadic that fully describes the relationship between the electric field and the induced current at the scatterer [15]. In (14), $\mathbf{E}(\mathbf{r})$ denotes the total electrical field, which is $\mathbf{E}(\mathbf{r}) = \mathbf{E}_i(\mathbf{r}) + \mathbf{E}_s(\mathbf{r})$, having indicated with $\mathbf{E}_i(\mathbf{r})$ the electrical field incident to the scatterer generated by the source in the absence of the scatterer and with $\mathbf{E}_s(\mathbf{r})$ the scattered field caused by the induced current $\mathbf{J}_s(\mathbf{r})$.

Suppose we aim to solve the EM problem of determining the total electric field $\mathbf{E}(\mathbf{r})$ and/or its scattered component $\mathbf{E}_s(\mathbf{r})$ when the scattering device is illuminated by an EM source. Both the

³A more general treatment is based on the equivalent principle where fictitious electric and magnetic currents are introduced as a function of the tangent electric and magnetic fields [15]. For clarity, hereby we focus on a more limited case valid for dielectric and non-perfect conductors.

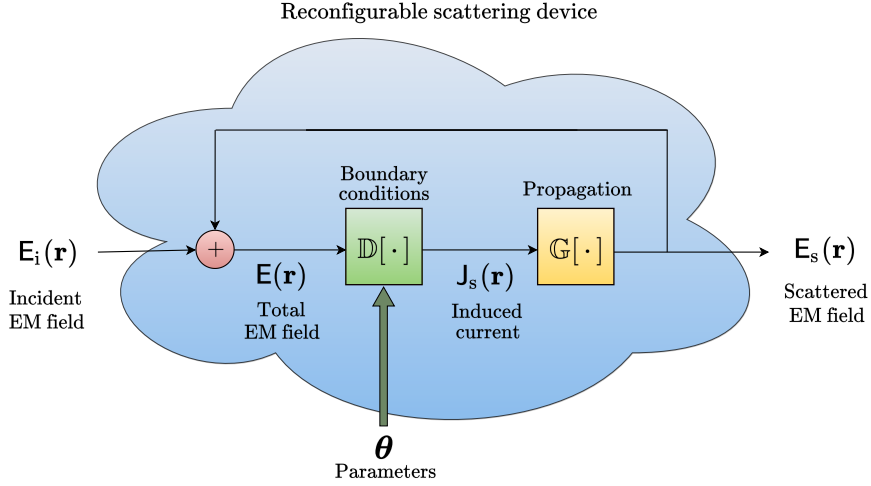


Fig. 4. The reconfigurable scattering device as a space-variant feedback filter.

electric field and the current must satisfy the free-space propagation equation (1) and the constitutive equation (14), which imposes a boundary condition. Examining the relationship between (1) and (14), it is noteworthy that any scattering device can be viewed as a feedback system, as illustrated in Fig. 4. In this framework, $E_i(\mathbf{r})$ represents the input, the propagation operator \mathbb{G} acts as a space-invariant filter, filtering the wavenumber components of the electric field within the support \mathcal{E} , as defined in (6), and the scattering device itself functions as a space-variant filter \mathbb{D} (analogous to time-variant filters), with the induced current $J_s(\mathbf{r})$ as its output. The filter \mathbb{D} can be designed through the parameters θ , i.e., $\mathbb{D}(\theta)$.

The analysis of the feedback system in Fig. 4 leads to integral equations, the solution of which is generally a complex problem that is typically tackled numerically. A more efficient approach is to use the method of moments, which involves expressing the fields and currents as series expansions using appropriately defined basis sets [37]. To this end, let $\{\Phi_k(\mathbf{r})\}_{k=1}^K$ denote a complete orthonormal vector basis set for \mathcal{S} , which depends solely on the geometry of \mathcal{S} . In general, K is infinite for the basis set to be complete, but K can be set to a sufficiently large finite value based on the desired level of accuracy. Consequently, the current density $J_s(\mathbf{r})$, the incident and scattered electric fields $E_i(\mathbf{r})$, $E_s(\mathbf{r})$, and the total electric field $E(\mathbf{r})$ within the space \mathcal{S} , i.e., for $\mathbf{r} \in \mathcal{S}$, can be expressed as a linear combination of these basis functions, namely

$$J_s(\mathbf{r}) = \sum_{k=1}^K [j_s]_k \Phi_k(\mathbf{r}), \quad E_i(\mathbf{r}) = \sum_{k=1}^K [e_i]_k \Phi_k(\mathbf{r}), \quad E_s(\mathbf{r}) = \sum_{k=1}^K [e_s]_k \Phi_k(\mathbf{r}), \quad E(\mathbf{r}) = \sum_{k=1}^K [e]_k \Phi_k(\mathbf{r}) \quad (15)$$

where the complex coefficients $\{[j_s]_k\}$ composing the vector \mathbf{j}_s are given by $[j_s]_k = \langle J_s(\mathbf{r}), \Phi_k(\mathbf{r}) \rangle$, for $k = 1, 2, \dots, K$. The vectors \mathbf{e}_i , \mathbf{e}_s , and \mathbf{e} are defined analogously, containing the coefficients of the

series expansions of, respectively, $\mathbf{E}_i(\mathbf{r})$, $\mathbf{E}_s(\mathbf{r})$, and $\mathbf{E}(\mathbf{r})$, according to the same basis set $\{\Phi_k(\mathbf{r})\}$. The vectors \mathbf{j}_s , \mathbf{e}_i , \mathbf{e}_s , and \mathbf{e} represent generalized currents and voltages. When the scattering device consists of a set of radiating elements (e.g., dipoles), each with a programmable loaded port, a suitable choice of the functions $\{\Phi_k(\mathbf{r})\}$ allows \mathbf{j}_s and \mathbf{e}_s to be directly associated with the actual currents and voltages at the ports. This effectively maps the original problem into an electrical circuit model (see Sec. V-A).

From Fig. 4, it is straightforward to write $\mathbf{E}(\mathbf{r}) = \mathbf{E}_i(\mathbf{r}) + (\mathbb{G}\mathbf{J}_s)(\mathbf{r}) = \mathbf{E}_i(\mathbf{r}) + (\mathbb{G}\mathbb{D}\mathbf{E})(\mathbf{r})$. As a consequence, $\mathbf{e} = \mathbf{e}_i + \mathbf{e}_s = \mathbf{e}_i + \mathbf{G}\mathbf{j}_s = \mathbf{e}_i + \mathbf{G}\mathbf{D}\mathbf{e}$, where $\mathbf{G} \in \mathbb{C}^{K \times K}$ is a matrix accounting for the self-coupling of the scattering device having elements $[\mathbf{G}]_{i,k} = \langle \Phi_i(\mathbf{r}), (\mathbb{G}\Phi_k)(\mathbf{r}) \rangle$ for $i, k = 1, 2, \dots, K$, and $\mathbf{D} \in \mathbb{C}^{K \times K}$ is a matrix with elements $[\mathbf{D}]_{i,k} = \langle \Phi_i(\mathbf{r}), (\mathbb{D}\Phi_k)(\mathbf{r}) \rangle$, for $i, k = 1, 2, \dots, K$. It follows that

$$\mathbf{e}_s = \mathbf{G}\mathbf{j}_s = \mathbf{G}\mathbf{D}(\mathbf{I}_K - \mathbf{G}\mathbf{D})^{-1}\mathbf{e}_i = \mathbf{R}\mathbf{e}_i \quad (16)$$

where \mathbf{I}_K is the identity matrix of size K , and $\mathbf{R} = \mathbf{R}(\theta) = \mathbf{G}\mathbf{D}(\mathbf{I}_K - \mathbf{G}\mathbf{D})^{-1}$ serves as the *reflection matrix* (or *scattering matrix* in the electromagnetic community). Specifically, the (k, i) -th element of \mathbf{R} represents the reflection coefficient corresponding to the k -th component of the impinging electric field and the i -th component of the scattered field, as described by the basis set $\{\Phi_k(\mathbf{r})\}$. Notably, depending on the available technology, the matrix \mathbf{D} might be constrained to take a particular structure. For example, if we exclude the presence of non-reciprocal materials in the scatterer, the response of the scattering device must verify the reciprocity theorem, hence resulting in a symmetric matrix [40]. Another example is the case where the boundary conditions imposed by the reconfigurable scatterer are local, i.e., $\mathbf{D}(\mathbf{r}, \mathbf{s}) = \mathbf{D}(\mathbf{r})\delta(\mathbf{r} - \mathbf{s})$ and hence $\mathbf{J}_s(\mathbf{r}) = \mathbf{D}(\mathbf{r})\mathbf{E}(\mathbf{r})$ in (14) [15]. For instance, if we consider the reconfigurable scattering device to be composed of a set of K uncoupled discrete elements each described by the k -th function $\Phi_k(\mathbf{r})$ of the basis set, the $\{\Phi_k(\mathbf{r})\}$'s are disjoint functions, and hence matrix \mathbf{D} is restricted to be diagonal as well as the reflection matrix \mathbf{R} being the elements uncoupled by assumption (see Sec. V for examples).

With reference to Fig. 3, let us now consider two distinct coupling problems: from the source space \mathcal{S}_T to the scattering device space \mathcal{S} , and from the scattering device space to the receiving space \mathcal{S}_R , both involving the operator \mathbb{G} . A direct coupling between the source and receiving spaces may occur; however, the reconfigurable scattering device cannot control this interaction. Therefore, unless otherwise specified, we will focus solely on the EM field component received from the scattering device.

Suppose the communication modes associated with the first link (from the source space to the scattering device) and the second link (from the scattering device to the receiving space) have been derived through the coupled eigenfunction problems (11) by truncating the series to the first K

$$\mathbf{C} = \begin{matrix} & \begin{matrix} \text{Sphere} & \text{Sphere} & \text{Sphere} & \text{Sphere} & \dots \end{matrix} \\ \begin{matrix} \text{Sphere} \\ \text{Sphere} \\ \text{Sphere} \\ \text{Sphere} \\ \vdots \end{matrix} & \left[\begin{array}{ccccc} C_{1,1} & C_{1,2} & C_{1,3} & C_{1,4} & \dots \\ C_{2,1} & C_{2,2} & C_{2,3} & C_{2,4} & \dots \\ C_{3,1} & C_{3,2} & C_{3,3} & C_{3,4} & \dots \\ C_{4,1} & C_{4,2} & C_{4,3} & C_{4,4} & \dots \\ \vdots & \vdots & \vdots & \vdots & \ddots \end{array} \right] \end{matrix}$$

Fig. 5. The reconfigurable scattering device as a mode converter. The spheres represent the input and output basis functions.

terms, where K is sufficiently large. Denote with $\left(\left\{\varphi_n^{(T)}(\mathbf{r})\right\}, \left\{\Psi_n^{(T)}(\mathbf{r})\right\}, \sigma_n^{(T)}\right)$ the n -th basis couple and singular value of the first link, for $n = 1, 2, \dots, K$, and with $\left(\left\{\varphi_m^{(R)}(\mathbf{r})\right\}, \left\{\Psi_m^{(R)}(\mathbf{r})\right\}, \sigma_m^{(R)}\right)$ the m -th basis couple and singular value of the second link, for $m = 1, 2, \dots, K$. Denote with $\mathbf{G}_T = \text{diag}\left(\sigma_1^{(T)}, \sigma_2^{(T)}, \dots, \sigma_K^{(T)}\right) \in \mathbb{C}^{K \times K}$ and $\mathbf{G}_R = \text{diag}\left(\sigma_1^{(R)}, \sigma_2^{(R)}, \dots, \sigma_K^{(R)}\right) \in \mathbb{C}^{K \times K}$ the coupling matrices between, respectively, the source and device spaces, and the device and receiving spaces. The effect of the scattering device can be fully described by the device operator $\mathbf{C} = \mathbf{C}(\boldsymbol{\theta}) \in \mathbb{C}^{K \times K}$, whose generic element $[\mathbf{C}]_{m,n}$ represents the coupling coefficient between the input communication mode n and the output communication mode m . As a consequence, the end-to-end coupling between the source space and the receiving space is given by

$$\mathbf{H}(\boldsymbol{\theta}) = \mathbf{G}_R \mathbf{C}(\boldsymbol{\theta}) \mathbf{G}_T. \quad (17)$$

The device operator $\mathbf{C}(\boldsymbol{\theta})$, also known as the *mode transfer matrix*, is determined by the specific structure and technology of the scattering device, as well as its configuration parameters $\boldsymbol{\theta}$, which enable the realization of different end-to-end processing functionalities $\mathbf{H}(\boldsymbol{\theta})$. In essence, any linear scattering device can be seen as a *mode converter* (see Fig. 5) [39].

We now derive the relationship between $\mathbf{C}(\boldsymbol{\theta})$ and $\mathbf{D}(\boldsymbol{\theta})$. By defining $\mathbf{U} \in \mathbb{C}^{K \times K}$, with elements $[\mathbf{U}]_{m,k} = \left\langle \varphi_m^{(R)}(\mathbf{r}), \Phi_k(\mathbf{r}) \right\rangle$ as the transformation matrix between the basis $\left\{\varphi_m^{(R)}(\mathbf{r})\right\}$ and $\left\{\Phi_k(\mathbf{r})\right\}$, and $\mathbf{V} \in \mathbb{C}^{K \times K}$, with elements $[\mathbf{V}]_{n,k} = \left\langle \Psi_n^{(T)}(\mathbf{r}), \Phi_k(\mathbf{r}) \right\rangle$, the transformation matrix between the basis $\left\{\Phi_k(\mathbf{r})\right\}$ and $\left\{\Psi_n^{(T)}(\mathbf{r})\right\}$, we can write

$$\mathbf{C}(\boldsymbol{\theta}) = \mathbf{U} \mathbf{D}(\boldsymbol{\theta}) (\mathbf{I}_K - \mathbf{G} \mathbf{D}(\boldsymbol{\theta}))^{-1} \mathbf{V}^{-1}. \quad (18)$$

It is useful to examine how (18) simplifies under the assumption of weak reflections, i.e., when $|\mathbf{E}_s(\mathbf{r})| \ll |\mathbf{E}_i(\mathbf{r})|$ for $\mathbf{r} \in \mathcal{S}$, which corresponds to $\|\mathbf{G} \mathbf{D}(\boldsymbol{\theta})\| \ll 1$. Specifically, we have

$$\mathbf{C}(\boldsymbol{\theta}) \approx \mathbf{U} \mathbf{D}(\boldsymbol{\theta}) \mathbf{V}^{-1}. \quad (19)$$

This corresponds to the Born approximation, which involves using the incident field as the driving field at each point in the scattering device, rather than the total EM field. This approximation is valid when the scattered field is small relative to the incident field on the scattering device. Notably, this result is equivalent to removing the feedback loop in Fig. 4. Depending on the specific technology being analyzed, the use of the approximation (19) instead of (18) should be considered with caution, as it may fail to capture important physical phenomena. An example of this is the Floquet modes in periodic metamaterials, which correspond to spurious reflections in undesired directions [15], [22].

In conclusion, the ESP problem can be framed as finding the optimal configuration parameter set θ that best approximates a given objective end-to-end processing functionality \mathbf{H}_o according to a specific criterion. This can be formulated as the following minimization problem:

$$\hat{\theta} = \arg \min_{\theta} \|\mathbf{G}_R \mathbf{C}(\theta) \mathbf{G}_T - \mathbf{H}_o\|_F \quad (20)$$

subject to a constraint on the radiated power, where $\|\cdot\|_F$ denotes the Frobenius norm. Depending on the adopted technology, additional constraints should be incorporated into the minimization problem to account for the specific structure and symmetries of the matrix $\mathbf{D}(\theta)$ and hence $\mathbf{C}(\theta)$. This underscores the need for tailored optimization algorithms based on physically consistent models. In this regard, specific examples will be provided in Sec. V-B.

IV. FUNDAMENTAL LIMITS

The ultimate limit in terms of the number of DoF, i.e., the flexibility of the reconfigurable scattering device to produce the desired EM response, can be obtained supposing that through a proper configuration of the device and illumination from the source space, it is possible to generate any induced current distribution on \mathcal{S} . In the following, we see that even in the case of an unbounded space (infinite receiver's size), the number of DoF is limited by the size of the scattering device compared to the wavelength. This number of DoF is further limited when finite source and receiver spaces are considered. In any case, these theoretical limits have to be intended as upper bounds because the particular technology considered might pose further constraints.

A. DoF in the Unbounded Space

In the following, we revisit the main results regarding the number of DoF for the radiating EM field in an unbounded space, given a current density $\mathbf{J}(\mathbf{r})$ defined within a limited space \mathcal{S} , using signal processing arguments.

1) *DoF for 1D Structures:* In this case, \mathcal{S} is a line segment of length L with coordinate $r_x \in [-L/2, L/2]$. Without loss of generality, we consider vertical EM waves polarization. Suppose $\mathbf{J}(\mathbf{r}) = J(r_x) \delta(r_y) \delta(r_z) \hat{\mathbf{y}}$ defined in \mathcal{S} . It is $\tilde{\mathbf{J}}(\boldsymbol{\kappa}) = \mathcal{F}_3[\mathbf{J}(\mathbf{r})] = \mathcal{F}[J(r_x)] \hat{\mathbf{y}} = \tilde{J}(\kappa_x) \hat{\mathbf{y}} = \tilde{\mathbf{J}}(\kappa_x)$, where

$\tilde{J}(\kappa_x) = \mathcal{F}[J(r_x)]$. It is well-known that every function $J(r_x)$ limited in $[-L/2, L/2]$ can be represented as an infinite series expansion of Fourier basis functions (i.e., modes)

$$J(r_x) = \sum_{n=-\infty}^{\infty} j_n \cdot \frac{1}{\sqrt{L}} \text{Rect}\left(\frac{r_x}{L}\right) e^{j k_n r_x} \quad (21)$$

where $k_n = 2n\pi/L$ and $\text{Rect}(x) = 1$, for $|x| < 0.5$, and zero otherwise. Then it is

$$\tilde{J}(\kappa_x) = \sum_{n=-\infty}^{\infty} j_n \sqrt{L} \text{Sinc}\left(\frac{L}{2\pi}(\kappa_x - k_n)\right) \quad (22)$$

being $\text{Sinc}(x) = \sin(\pi x)/(\pi x)$. Note that, according to (6), only the modes for which $|k_n| \leq k_0 = 2\pi/\lambda$ radiate. Then, only $N = 2L/\lambda$ terms in (22) fall in the visible region.⁴ Being the wavenumber support limited (i.e., $\tilde{J}(\kappa_x)$ band limited in $[-k_0, k_0]$), we can say that any EM radiated field that can be generated by a current line source of length L can be fully represented by sampling it in the wavenumber domain at frequencies $k_n = 2n\pi/L$ for $|n| \leq N/2$. Thus, the required number N of samples leads to the DoF in the unbounded space, that is, $DoF = \frac{2L}{\lambda}$ (per polarization). To draw a parallel, when beamforming is operated using N half-wavelength spaced antennas arranged as a uniform linear array (ULA), N orthogonal beams (i.e., $2L/\lambda$ when the antenna spacing is $\lambda/2$) can be realized. These can be adopted to reach users in every possible angular direction (e.g., for initial access). These beams correspond to the set of orthogonal transmission directions that can be spanned by the ULA considering the classical discrete Fourier transform (DFT)-based codebook of beamforming vectors given by

$$\frac{1}{\sqrt{N}} \left[1, e^{-j\frac{2\pi n}{N}}, e^{-j\frac{2\pi 2n}{N}}, \dots, e^{-j\frac{2\pi(N-1)n}{N}} \right]^T = \frac{1}{\sqrt{N}} \left[1, e^{-j\frac{k_n \lambda}{2}}, e^{-j\frac{2k_n \lambda}{2}}, \dots, e^{-j\frac{(N-1)k_n \lambda}{2}} \right]^T. \quad (23)$$

The different vectors correspond to the transmission directions towards angles $\gamma_n = \arcsin \frac{2n}{N}$, for $n = \pm 1, \pm 2, \dots, \lfloor \frac{N}{2} \rfloor$. The characteristic of these beams is that each one points towards the null directions of all the other beams. Every possible channel vector (i.e., direction) can be realized as a linear combination of the vectors in (23), which is an orthonormal basis for \mathbb{C}^N .

2) *DoF for 2D Structures*: In this second case, \mathcal{S} is a surface of size $L_x \times L_y$. Similarly to the 1D case, the current density can be represented as a 2D series expansion of Fourier basis functions. In the wavenumber domain, we have

$$\tilde{J}(\kappa_x, \kappa_y) = \sum_{n_x, n_y} j_{n_x, n_y} \sqrt{L_x L_y} \text{Sinc}\left(\frac{L_x}{2\pi}(\kappa_x - k_{n_x})\right) \text{Sinc}\left(\frac{L_y}{2\pi}(\kappa_y - k_{n_y})\right) \quad (24)$$

where $k_{n_x} = 2n_x\pi/L_x$, and $k_{n_y} = 2n_y\pi/L_y$. Note that only the set of indexes $(n_x, n_y) \in \mathcal{P}_2$, with $\mathcal{P}_2 = \left\{ (n_x, n_y) : \left(\frac{n_x \lambda}{L_x}\right)^2 + \left(\frac{n_y \lambda}{L_y}\right)^2 \leq 1 \right\}$, satisfying $k_{n_x}^2 + k_{n_y}^2 \leq k_0^2$, are not evanescent, i.e., lie in the visible region. For instance, for a square surface of size $L_x = L_y = L$, it is $DoF \simeq |\mathcal{P}_2| \simeq \frac{\pi L^2}{\lambda^2}$ (per

⁴More precisely, we assume that $L \gg \lambda$; otherwise, the tails of certain Sinc functions centered in the non-visible region could significantly contribute to the visible region.

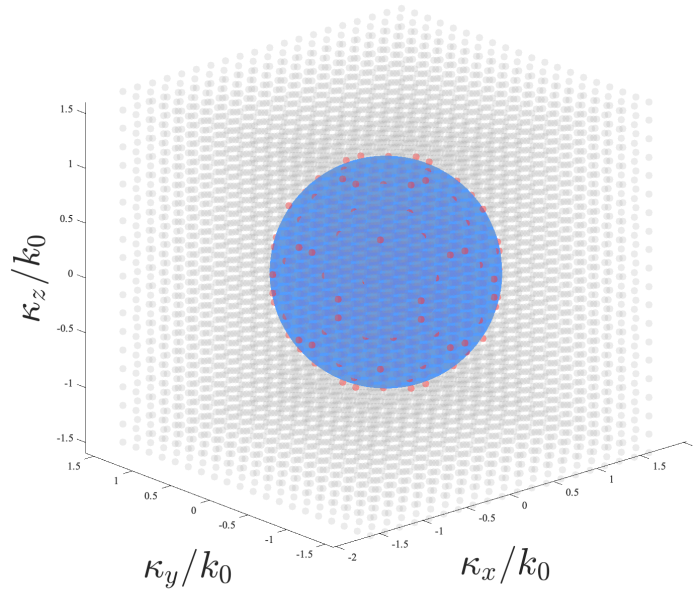


Fig. 6. Filtering operation of the Green propagation operator in the wavenumber domain for $L/\lambda = 6$. The sphere corresponding to the set \mathcal{E} is depicted in blue, while the grey points represent the 3D Sinc functions in (25). The red points instead denote the subset of 3D Sinc functions in (25) having significant intersection with the sphere, hence generating EM waves.

polarization) [15]. Interestingly, this is $\pi/4 = 0.79$ of the square of the DoF of a linear segment. As a consequence, by drawing a parallel as before with uniform planar arrays, we have that a $N \times N$ planar array will not be able to generate N^2 orthogonal beams (i.e., $\frac{4L^2}{\lambda^2}$), as could be erroneously suggested by intuition, but only the subset of $\frac{\pi}{4}N^2 \approx 0.79N^2$ beams satisfying the condition of non-evanescent modes.

3) *DoF for 3D Structures:* When \mathcal{S} is a volume of size $L_x \times L_y \times L_z$, in the wavenumber domain we have

$$\tilde{J}(\kappa_x, \kappa_y, \kappa_z) = \sum_{n_x, n_y, n_z} j_{n_x, n_y, n_z} \sqrt{L_x L_y L_z} \text{Sinc}\left(\frac{L_x}{2\pi}(\kappa_x - k_{n_x})\right) \text{Sinc}\left(\frac{L_y}{2\pi}(\kappa_y - k_{n_y})\right) \text{Sinc}\left(\frac{L_z}{2\pi}(\kappa_z - k_{n_z})\right) \quad (25)$$

where $k_{n_x} = 2\pi n_x/L_x$, $k_{n_y} = 2\pi n_y/L_y$, and $k_{n_z} = 2\pi n_z/L_z$.

The derivation of the number of DoF for a 3D structure is more involved. The typical approach is to consider the smallest sphere enclosing the space \mathcal{S} , define a complete basis set given by the spherical harmonic functions on its surface, and identify the N dominant ones [37]. Here we follow an approximate but simpler approach for the case $L_x = L_y = L_z = L$. The modes in (25) contributing to the EM field are those with index combinations (n_x, n_y, n_z) , corresponding to the wavenumber points $\boldsymbol{\kappa}_{n_x, n_y, n_z} = (k_{n_x}, k_{n_y}, k_{n_z})$, for which the intersection with the surface of radius k_0 defined in (6) is not negligible. Their number can be approximatively evaluated as the number of wavenumber

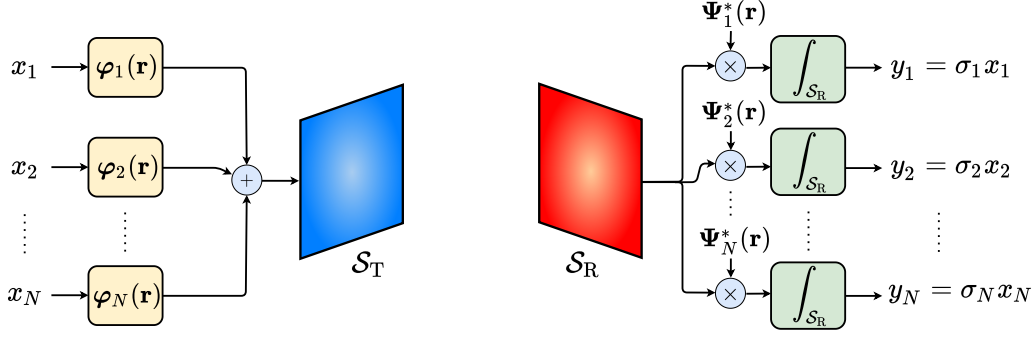


Fig. 7. Optimal communication scheme between spaces based on communication modes.

points κ_{n_x, n_y, n_z} falling within the shell of radius κ_0 and thickness δ (see Fig. 6). Denote with \mathcal{P}_3 the set of indexes (n_x, n_y, n_z) whose wavenumber satisfies this condition. For instance, δ can be taken equal to the first lobe of the Sinc function, i.e., $\delta = 2\pi/L$. Specifically, it is $DoF \simeq |\mathcal{P}_3| = \nu \cdot V_\delta$, where $\nu = (\frac{L}{2\pi})^3$ is the density of the wavenumber points and V_δ is the volume of the shell. Therefore, it is

$$DoF \simeq \nu \cdot V_\delta = \frac{\pi}{3} + \frac{4\pi L^2}{\lambda^2} \simeq \frac{\pi^2 L^2}{\lambda^2} \quad (26)$$

for $L \gg \lambda$, which is the same result one can obtain using a more precise but complex approach based on spherical harmonic waves. Note that using volumetric antennas than planar antennas a DoF gain of π can only be obtained. It can be pointed out that while for the 1D case sampling the current with spacing $\lambda/2$ is necessary to represent the current components contributing to the radiating EM field, in the 2D and 3D cases sampling at $\lambda/2$ is only a sufficient but no longer necessary condition. Readers can refer to [41] for a more detailed discussion.

B. DoF of the Single Link

Consider a communication system involving a transmitting space \mathcal{S}_T and a receiving space \mathcal{S}_R . Each space allows for a maximum number of DoF in the unbounded space, as discussed in Sec. IV-A. However, only a subset of these available DoF can be exploited for communication, corresponding to the N well-coupled communication modes with eigenvalues σ_n^2 described in Sec. III-B. When currents are excited at \mathcal{S}_T corresponding to these well-coupled modes, the resulting EM field is predominantly concentrated on the receiver space \mathcal{S}_R . In contrast, exciting modes outside this subset of well-coupled modes leads to an EM field largely dispersed away from \mathcal{S}_R .

In the context of communication systems, the N communication modes represent the available DoF between the transmitting space \mathcal{S}_T and the receiving space \mathcal{S}_R , which can be modeled using the communication scheme shown in Fig. 7. Here, N information symbols $\mathbf{x} \in \mathbb{C}^N$ are associated with the basis functions $\{\varphi_n(\mathbf{r})\}$, forming the source current density $\mathbf{J}(\mathbf{r}) = \sum_n x_n \varphi_n(\mathbf{r})$ on \mathcal{S}_T . At the receiver,

the information is recovered by correlating the received EM field $\mathbf{E}(\mathbf{r})$ with the corresponding basis functions $\{\Psi_n(\mathbf{r})\}$ on \mathcal{S}_R , i.e., $y_n = \langle \mathbf{E}(\mathbf{r}), \Psi_n(\mathbf{r}) \rangle$, resulting in a set of matched filters operating in the spatial domain. Formally, considering the effect of noise, the received signal $\mathbf{y} \in \mathbb{C}^N$ is given by the following equation

$$\mathbf{y} = \mathbf{\Sigma} \mathbf{x} + \mathbf{n} \quad (27)$$

where $\mathbf{\Sigma} = \text{diag}(\sigma_n) \in \mathbb{C}^{N \times N}$, $\mathbf{n} \in \mathbb{C}^N$ is the additive white Gaussian noise (AWGN) with $\mathbf{n} \sim \mathcal{CN}(\mathbf{0}, \sigma_{\text{noise}}^2 \mathbf{I}_N)$, where σ_{noise}^2 is the noise power and $\mathcal{CN}(\cdot, \cdot)$ denotes a multivariate complex normal distribution. Moreover, let \mathbf{Q} be the positive semi-definite (i.e., $\mathbf{Q} \geq 0$) covariance matrix of the transmitted signal, i.e., $\mathbf{Q} = \mathbb{E}[\mathbf{x}\mathbf{x}^H]$, where $\mathbb{E}[\cdot]$ is the expectation operator and $(\cdot)^H$ denotes the complex transpose. Then, the transmit power constraint is $\text{tr}(\mathbf{Q}) \leq P_T$, where $\text{tr}(\cdot)$ is the trace operator and P_T is the total transmit power.

As well-known from the MIMO theory, the transmitter must split its power among the N parallel single-input single-output (SISO) channels. For any \mathbf{Q} , the overall capacity is the sum of the capacities of the individual channels, leading to [42]

$$C = \max_{\substack{p_1 \geq 0, \dots, p_N \geq 0 \\ \text{tr}(\mathbf{Q}) \leq P_T}} \sum_{n=1}^N \log_2 \left(1 + \frac{p_n \sigma_n^2}{\sigma_{\text{noise}}^2} \right) \quad (28)$$

where the optimum power allocation follows the water-filling solution as per

$$p_n = \max \left(\mu - \frac{\sigma_{\text{noise}}^2}{\sigma_n^2}, 0 \right), \quad n = 1, \dots, N \quad (29)$$

and being the variable μ selected to fulfill the condition $\sum_{n=1}^N p_n = P_T$. The eigenvalues σ_n^2 represent the channel gains and, being ordered in decreasing magnitude, the power is allocated from the strongest to the weakest channels. Consequently, the number of significant eigenvalues (i.e., the number of DoF) and their distribution have a significant impact on the maximum capacity. A few examples are hereby provided.

1) *DoF for 1D Structures*: Consider two 1D segments, as described in Sec. IV-A, placed parallel to each other and aligned along their centers (i.e., in a paraxial configuration). We focus on a single polarization. The lengths of the segments are denoted as L_T and L_R , and the distance between their centers is d . It can be demonstrated that the N most significant eigenvalues in this configuration are nearly identical in magnitude and then rapidly decay. Therefore, according to the water-filling principle in (29), the power can be evenly distributed among the N modes. The number of DoF of the link, or the number of significant eigenvalues, can thus be determined for a single polarization as follows [39]

$$N = \frac{L_T L_R}{\lambda d}. \quad (30)$$

This classical expression, while accurately determining the number of DoF when $L_T, L_R \gg d$ and the sizes of L_T and L_R are nearly comparable, becomes inadequate when one of the segments grows excessively large. In fact, (30) appears to suggest that the DoF can increase indefinitely if either L_T or L_R becomes infinitely large. However, this contradicts the results obtained in Sec. IV-A, where the maximum number of DoF is bounded and cannot exceed the values derived for an unbounded space. A more accurate expression was derived in [43] by analyzing the scalar Green operator and modeling the communication modes as focused beams, which leads to

$$N = \frac{2L_T}{\lambda} \zeta \quad (31)$$

with $\zeta = L_R / \sqrt{4d^2 + L_R^2}$. From expression (31), it can be observed that as $L_R \rightarrow \infty$, we have $\zeta \rightarrow 1$, and thus the limit is $N = \frac{2L_T}{\lambda}$, which corresponds to the actual limit in the unbounded space presented in Sec. IV-A. Among the $N = \frac{2L_T}{\lambda}$ orthogonal beamsteering directions associated with (23) that can be generated with the segment of length L_T , (31) indicates the number of beams that intersect the parallel segment of length L_R at a distance d .

2) *DoF for 2D Structures*: Consider now two square surfaces with areas, respectively, $A_T = L_T^2$ and $A_R = L_R^2$, where $A_T < A_R$. These surfaces are located at a distance d in a paraxial configuration and outside the reactive region of the transmitting area. When $d > L_R$, the classical expression for the available DoF (per polarization) is [39]

$$N = \frac{A_T A_R}{\lambda^2 d^2}. \quad (32)$$

In [5], the following alternative expression is derived for $A_T < A_R$

$$N = \frac{4A_T}{\lambda^2} \zeta \tan^{-1} \zeta. \quad (33)$$

Unlike (32), (33) provides the actual number of DoF for squared planar paraxial surfaces of any size, also demonstrating a saturation when $d \ll L_R$. In the case $L_R \rightarrow \infty$, the limit is $N = \frac{\pi A_T}{\lambda^2}$, which matches the result obtained for the unbounded space in Sec. IV-A.

C. DoF of the Cascade Link

When a reconfigurable scattering device is placed between the transmitter and the receiver, as discussed in Sec. III-C and shown in Fig. 3, we define N and M as the maximum number of “usable” channels (i.e., communication modes) into and out of the scattering device, respectively. Here, N and M correspond to the rank of \mathbf{G}_T and \mathbf{G}_R , respectively, with $N, M \leq K$. The maximum number of end-to-end communication modes is given by $R = \min(N, M)$. The equivalent end-to-end channel can be written as

$$\mathbf{y} = \mathbf{H}(\boldsymbol{\theta}) \mathbf{x} + \mathbf{n} \quad (34)$$

where now $\mathbf{y}, \mathbf{x}, \mathbf{n} \in \mathbb{C}^K$, and the end-to-end channel matrix $\mathbf{H}(\theta)$ defined in (17) can be written equivalently as $\mathbf{H}(\theta) = \mathbf{G}_R \mathbf{U} \mathbf{G}^{-1} \mathbf{R}(\theta) \mathbf{V}^{-1} \mathbf{G}_T = \mathbf{H}_R \mathbf{R}(\theta) \mathbf{H}_T$, with $\mathbf{H}_R = \mathbf{G}_R \mathbf{U} \mathbf{G}^{-1}$ and $\mathbf{H}_T = \mathbf{V}^{-1} \mathbf{G}_T$, to explicit the effect of the reflection matrix $\mathbf{R}(\theta)$.

It is of interest to investigate the optimal configuration of the reconfigurable scattering device through the matrix $\mathbf{D}(\theta)$ (thus, $\mathbf{R}(\theta)$ and $\mathbf{H}(\theta)$) maximizing the end-to-end channel capacity given \mathbf{G}_T and \mathbf{G}_R under some constraint on the matrix $\mathbf{R}(\theta) \approx \mathbf{G} \mathbf{D}(\theta)$ (we make use of the Born approximation), for example, a lossless constraint for the reconfigurable scattering device⁵ leading to $\mathbf{R}(\theta) \mathbf{R}^H(\theta) = \mathbf{I}_K$.

Adopting the approach followed in [44], it can be proved that the end-to-end channel capacity of the reconfigurable scattering device-assisted communication is

$$C = \sum_{k=1}^K \log_2 \left(1 + \left(\tilde{\sigma}_k^{(T)} \right)^2 \left(\tilde{\sigma}_k^{(R)} \right)^2 \frac{p_k}{\sigma_{\text{noise}}^2} \right) \quad (35)$$

where $p_k = \max \left(\mu - \frac{\sigma_{\text{noise}}^2}{\left(\tilde{\sigma}_k^{(T)} \right)^2 \left(\tilde{\sigma}_k^{(R)} \right)^2}, 0 \right)$, with μ obtained by fulfilling the identity $\sum_{k=1}^K p_k = P_T$, and being $\tilde{\sigma}_k^{(T)}$ and $\tilde{\sigma}_k^{(R)}$ the singular values of \mathbf{H}_T and \mathbf{H}_R , respectively.⁶ It is important to note that the last $K - R$ power coefficients are zero due to the maximum rank of $\mathbf{H}(\theta)$ being R . Specifically, because of the diagonal structure of \mathbf{G}_T and \mathbf{G}_R , where only the first N and M diagonal entries, respectively, correspond to significant singular values, only the first R elements of the symbol vector \mathbf{x} (out of K) carry “usable” information data. In addition, (35) is obtained by setting $\mathbf{Q} = \text{diag}(p_1, p_2, \dots, p_K)$ and the coupling matrix $\mathbf{C} = \mathbf{I}_K$. Under the Born approximation, from (19), the optimal device matrix should satisfy the condition

$$\mathbf{R}(\theta) = \mathbf{V}_R \mathbf{U}_T^H \quad (36)$$

where \mathbf{V}_R and \mathbf{U}_T represent the left and right eigenvector matrices of the SVD of \mathbf{H}_T and \mathbf{H}_R , respectively. From (36), it can be inferred that the end-to-end capacity is maximized by designing $\mathbf{R}(\theta)$ (and consequently $\mathbf{D}(\theta)$) in a way that aligns with the left eigenvectors of the first link and the right eigenvectors of the second link. This ensures that the end-to-end transmitter-device-receiver channel is diagonalized. Furthermore, the water-filling power allocation is applied to the ordered product of the singular values of the individual transmitter-device and device-receiver channels.

The physical realizability of the optimal device matrix $\mathbf{R}(\theta)$ depends on the specific technology being used. As mentioned in Sec. III, when the boundary conditions imposed by the scattering device are local, such as in conventional RISs, the matrix $\mathbf{R}(\theta)$ is constrained to be diagonal, meaning that

⁵In this case, the power of the incident electric field \mathbf{e}_i equals that of the scattered electric field $\mathbf{e}_s = \mathbf{R}(\theta) \mathbf{e}_i$.

⁶We have $\tilde{\sigma}_k^{(T)} = \sigma_k^{(T)}$, since \mathbf{V} is unitary. In contrast, $\tilde{\sigma}_k^{(R)}$ may differ from $\sigma_k^{(R)}$ due to the presence of the matrix \mathbf{G}^{-1} in \mathbf{H}_R , which accounts for the coupling between the current density and the scattered electric field at the reconfigurable scattering device.

(36) can only be approximated [44]. Recently, new RIS structures have been introduced, which enable reconfigurable coupling between the elements, leading to a non-diagonal matrix (non-diagonal RISs) [45].

V. ENABLING EM TECHNOLOGIES AND SP CHALLENGES

In this section, we provide a comprehensive overview of key EM enabling technologies that can be utilized within the ESP framework by presenting specific examples of their application in practical processing tasks.

A. Port-controlled Reconfigurable Scattering Devices

In most practical implementations, the reconfigurable scattering device is composed of a discrete set of K antenna elements located at positions \mathbf{r}_k whose scattering characteristics can be adjusted by changing the load at their port. With a limited loss of generality, for a given k -th antenna element of the reconfigurable scattering device, define $\mathbf{F}_k(\mathbf{r})$ [$1/m^2$] the corresponding current density normalized to 1 [A] current at its input port. Here we are implicitly assuming that the antenna element can be characterized by only one dominant mode which is a good approximation, for instance, for Hertzian dipoles and resonant structures such as the half-wave dipole. The function $\mathbf{F}_k(\mathbf{r})$ depends on the particular structure of the element as well as its position \mathbf{r}_k and orientation. Such a distribution can be obtained in general through EM-based simulations, but closed-form expressions are available for simple structures such as Hertzian or half-wave dipoles [35]. The entire scattering device can be considered as a linear K -port network where we define the complex voltage and current envelopes (in the following denoted simply as voltages and currents) at the ports, respectively, \mathbf{v} (open circuit voltage) and \mathbf{i}_s . The actual current density of the k -th element is therefore $\mathbf{J}_{sk}(\mathbf{r}) = [\mathbf{i}_s]_k \cdot \mathbf{F}_k(\mathbf{r})$. The corresponding unitary-energy basis function is $\Phi_k(\mathbf{r}) = \mathbf{F}_k(\mathbf{r}) / \|\mathbf{F}_k(\mathbf{r})\|$, where $\|\mathbf{F}_k(\mathbf{r})\| = \sqrt{\langle \mathbf{F}_k(\mathbf{r}), \mathbf{F}_k(\mathbf{r}) \rangle}$. For simplicity, in the following, we consider the same structure for all elements so that $\|\mathbf{F}_k(\mathbf{r})\| = \alpha, \forall k$. As a consequence, the relationship between \mathbf{j}_s and \mathbf{i}_s is $\mathbf{j}_s = \alpha \mathbf{i}_s$, and the total current density can be expressed as a function of the ports' currents

$$\mathbf{J}(\mathbf{r}) = \sum_{k=1}^K \mathbf{J}_{sk}(\mathbf{r}) = \sum_{k=1}^K [\mathbf{i}_s]_k \alpha \Phi_k(\mathbf{r}). \quad (37)$$

Exploiting the reciprocity theorem, the open circuit voltage at the k -th element's port is $[\mathbf{v}]_k = \alpha \langle \mathbf{E}(\mathbf{r}), \Phi_k(\mathbf{r}) \rangle = \alpha [\mathbf{e}]_k$.

In the case of a Hertzian dipole of infinitesimal length $l \ll \lambda$ located at position \mathbf{r}_k with a generic polarization (orientation) $\hat{\mathbf{p}}_k$, the corresponding basis set is $\Phi_k(\mathbf{r}) = \hat{\mathbf{p}}_k \delta(\mathbf{r} - \mathbf{r}_k)$. The current and open circuit voltage at the ports are, respectively, $\mathbf{v} = l \mathbf{e}$ and $\mathbf{j}_s = l \mathbf{i}_s$.

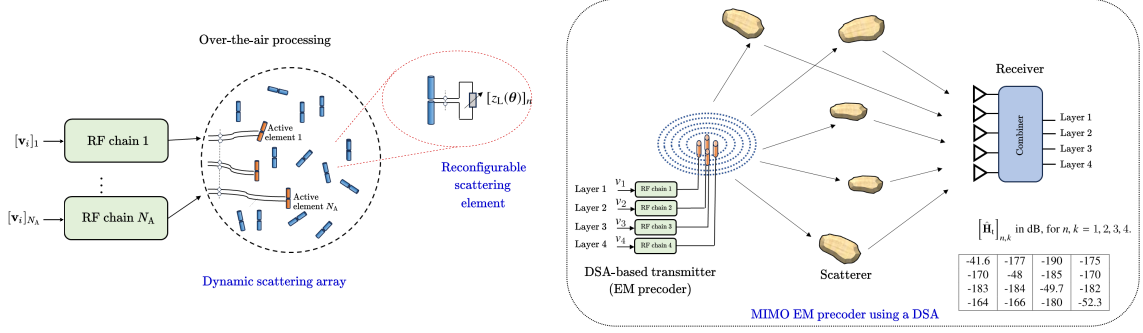


Fig. 8. The generic DSA structure with N_A RF chains and N_A active elements surrounded by N_S reconfigurable scattering elements. Example of MIMO communication in which the DSA is adopted at the transmitter.

B. EM Signal Processing in the Reactive Near Field

We illustrate here two examples related to the use of the general framework in Sec. III to model and design a dynamic scattering array (DSA) and a stacked intelligent metasurface (SIM) whose aim is to realize a given signal processing task at the EM level and minimize the number N_A of RF chains.

1) *Dynamic Scattering Arrays*: With reference to Fig. 8, a DSA is composed of K antenna elements (e.g., dipoles) located within the space \mathcal{S} of which N_A are active and hence connected to an RF chain, and $N_S = K - N_A$ are passive scattering antenna elements [20], [29], [30], [46]. The response of the DSA can be changed by loading each scattering antenna element with reconfigurable loads of impedances $\mathbf{z}_L = \mathbf{z}_L(\boldsymbol{\theta})$. Ideally, the loads are designed to be only reactive to avoid power losses, i.e., $\mathbf{z}_L = j\boldsymbol{\theta}$, with $\boldsymbol{\theta} \in \mathbb{R}^K$. Now, the N_A RF chains introduce impressed open circuit voltages $\mathbf{v}_i = [v_1, v_2, \dots, v_{N_A}, 0, 0, \dots, 0]^T$ to the first N_A elements that carry the information and are responsible for the impressed field \mathbf{e}_i . In particular, in Sec. III we have seen that it should be $\mathbf{e} = \mathbf{e}_i + \mathbf{e}_s$, where $\mathbf{e} = \mathbf{D}^{-1}\mathbf{j}_s$ and $\mathbf{e}_s = \mathbf{G}\mathbf{j}_s$. Moreover, since $\{\Phi_k(\mathbf{r})\}$'s are disjoint functions, then \mathbf{D} is diagonal. By multiplying the first relationship by the constant α defined in Sec. V-A, it is possible to map it into a relationship between currents and voltages at the ports, i.e., $\alpha^2 \mathbf{D}^{-1}\mathbf{i}_s = \mathbf{v}_i + \alpha^2 \mathbf{G}\mathbf{i}_s$. After simple steps, we obtain

$$(j \text{diag}(\boldsymbol{\theta}) - \mathbf{Z}) \mathbf{i}_s = \mathbf{v}_i \quad (38)$$

where $\mathbf{Z} = \alpha^2 \mathbf{G}$ is the impedance matrix of the antenna structure and $\mathbf{z}_L(\boldsymbol{\theta}) = j \text{diag}(\boldsymbol{\theta}) = \mathbf{D}^{-1}$ represents the set of reconfigurable loads' impedance. All the interactions between the elements of the DSA are captured by the impedance matrix \mathbf{Z} , which does not depend on the reconfigurable loads, and relates the voltages and currents of the K ports [35]. With Hertzian dipoles, it can be computed analytically as $[\mathbf{Z}]_{n,k} = l^2 \hat{\mathbf{p}}_n \cdot \mathbf{G}(\mathbf{r}_n - \mathbf{r}_k) \hat{\mathbf{p}}_k$, with $\mathbf{G}(\mathbf{r})$ given by (2).

For a given receiver space, the end-to-end mapping between the open circuit voltage at the N_A ports and the observed field \mathbf{y} is

$$\mathbf{y} = \alpha \mathbf{G}_R \mathbf{U} (J \text{diag}(\boldsymbol{\theta}) - \mathbf{Z})^{-1} \mathbf{v}_i. \quad (39)$$

The previous equation can be used as a general model for the DSA in an optimization problem once the desired response \mathbf{y} is fixed.

One design approach is named *characteristic mode analysis* and consists of designing $\boldsymbol{\theta}$ such that the current \mathbf{i}_s , needed to obtain the desired response \mathbf{y} , represents the dominant scattering mode of the structure. This can be simply accomplished by selecting $\boldsymbol{\theta}$ such that the current \mathbf{i}_s resonates, i.e., $[\boldsymbol{\theta}]_k = \frac{1}{[\mathbf{i}_s]_k} [\Im\{\mathbf{Z}\}\mathbf{i}_s]_k$, for $k = 1, 2, \dots, K$, where $\Im\{x\}$ denotes the imaginary part of x . This approach, originally proposed in [19], has been widely exploited for the design of ESPARs with a single RF chain [29], [46]. Unfortunately, this simple approach is not accurate when applied to large structures in which secondary modes might deviate from the actual response from the desired one, and it is not applicable in the case of multiple active antennas.

More in general, one might want to solve the following constrained optimization problem for a given objective end-to-end channel matrix $\mathbf{H}_o \in \mathbb{C}^{M \times N_A}$

$$\hat{\boldsymbol{\theta}} = \arg \min_{\boldsymbol{\theta}} \left\| \alpha \mathbf{G}_R \mathbf{U} (J \text{diag}(\boldsymbol{\theta}) - \mathbf{Z})^{-1} - \mathbf{H}_o \right\|_F \quad (40)$$

constrained to a fixed radiated power $P_T = \mathbf{i}_s^H \Re\{\mathbf{Z}\} \mathbf{i}_s$ [30], where $\Re\{x\}$ denotes the real part of x . The k -th row of \mathbf{H}_o represents the desired end-to-end channel response associated with the n -th port of the DSA. It is worth noticing that with the same configuration $\hat{\boldsymbol{\theta}}$ of the DSA, N_A different responses are obtained simultaneously, each one associated with the input port of one specific RF chain.

We illustrate a numerical example in which (40) is optimized to realize a MIMO EM precoder. In particular, we consider a MIMO communication in which the DSA is adopted at the transmitter as illustrated in Fig. 8. A receiving user equipped with a standard ULA with $K = 20$ elements spaced of $\lambda/2$ is located at 10 m in non-line-of-sight (NLOS) condition. The simulated NLOS channel consists of 5 multi-paths caused by the reflection of 5 scatterers in the environment located at angles $\phi = \{-43^\circ, -14^\circ, 14^\circ, 43^\circ, 72^\circ\}$ and distance 5 m. The corresponding strongest singular values of the channel are $(-35.6 \text{ dB}, -42.4 \text{ dB}, -43.7 \text{ dB}, -46.3 \text{ dB}, -82 \text{ dB}, \dots)$, which has clearly rank $r = 4$. The DSA is equipped with $N_S = 121$ Hertzian reconfigurable scattering dipoles deployed in 5 concentric rings and spaced apart of $\lambda/4$. The carrier frequency is 28 GHz so that the total size of the DSA is 3.2 cm. It is well-known from MIMO theory that for a given generic propagation scenario characterized by rank r , up to r parallel orthogonal links (layers) can be established between the transmitter and the receiver on which independent data stream can be transmitted [42]. To exploit all of them, the

number of active antennas (i.e., RF chains) must be $N_A = r$ and the DSA must implement a suitable precoding strategy, i.e., act as an *EM precoder*. Specifically, setting the target end-to-end channel to be diagonal and matching the singular values of the link $\mathbf{H}_0 = \alpha \mathbf{G}_R$ (channel diagonalization), must be

$$(\mathbf{J} \text{diag}(\boldsymbol{\theta}) - \mathbf{Z})^{-1} \propto \mathbf{U}^H \quad (41)$$

where \mathbf{U}^H represents the optimal precoding matrix. The resulting end-to-end matrix $\hat{\mathbf{H}}_0$, obtained by solving (41) numerically while maximizing the radiated power P_T (see [30] for the details), is reported in Fig. 8. The comparison between the diagonal and off-diagonal values indicates that the coupling between different layers is completely negligible, i.e., the channel is almost perfectly diagonalized. Compared to the actual singular values of the channel, the intensity of the diagonal elements of $\hat{\mathbf{H}}_0$ exhibit the same behavior with a loss of about 6 dB that can be ascribed to the fact that the antenna is not ideal. The designed DSA implements the optimal precoding at the EM level by using no more than $N_A = r$ RF chains (i.e., the minimum possible value) which is much simpler and less energy-consuming than any conventional full digital or hybrid solution by considering that the reconfigurable scattering elements are passive. Further examples of DSA design for the realization of superdirective beamforming and multi-user multiple-input single-output (MISO) can be found in [30]. The main challenge from the SP perspective lies in finding efficient techniques to tackle high-dimensional optimization problems constrained by EM laws like that in (40) for a large number of reconfigurable scattering elements.

2) *Stacked Intelligent Metasurfaces*: Recently, a new technology known as SIM has gained significant attention within the research community due to its advantages and potential applications [33]. A SIM consists of a sealed vacuum structure that incorporates multiple layers of metasurfaces, each containing many reconfigurable meta-atoms, i.e., small reconfigurable scattering elements, which are interconnected with a controller, e.g., a field programmable gate array (FPGA). Operating on the well-established Huygens-Fresnel principle, when an EM wave interacts with a meta-atom in any given layer, it acts as a secondary point source, illuminating all subsequent meta-atoms in the following layer. This architectural approach, which can be seen as a particular case of DSAs, with cells organized in layers and coupling occurring in only one direction, provides greater flexibility in EM waveform manipulation and enhanced spatial-domain gain when compared to conventional MIMO architectures, e.g., transmitarrays and hybrid MIMO antennas [47]. It significantly reduces the number of required RF chains, hence allowing for improved EM-level processing with very limited energy consumption [48].

Interestingly, thanks to their peculiar layered structure, several optimization algorithms for determining the optimal SIM transmission coefficients have been inspired by the well-known error

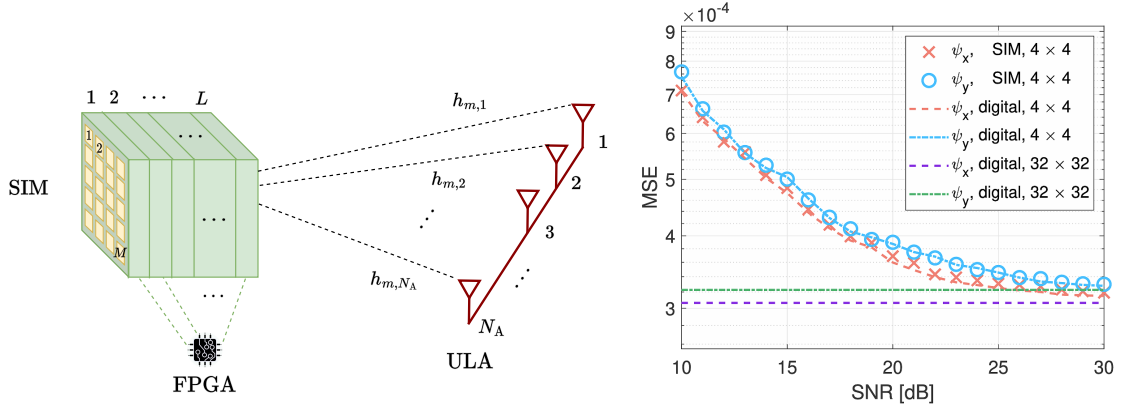


Fig. 9. SIM-based antenna architecture, comprising a ULA, L metasurface layers, and a FPGA for reconfigurability. Example of performance comparison of the SIM-based DoA estimator and the conventional approach via a 2D digital DFT [53].

backpropagation algorithm used for DNN training, hence leveraging their particular hardware architecture [49]. These algorithms allow for the optimization of the meta-atom configuration and the phase shifts imposed on EM waves passing through these structures. Such optimizations enable the implementation of various wave-domain functionalities, such as beamforming, precoding, and combining. For instance, [49] applied deep reinforcement learning to jointly optimize the phase shifts of SIMs and the transmit power allocation. In a complementary approach, [50] proposed a projected gradient descent (PGD) method to iteratively optimize the phase shifts of SIMs at the transceivers layer-by-layer, aimed at minimizing the channel cutoff rate under practical modulation constraints. Furthermore, [51] introduced a hybrid digital and wave-domain SIM-based MIMO transceiver architecture and proposed a projected gradient ascent (PGA) method that jointly optimizes the phase shifts of the SIM, alongside digital transmit precoding and receive combining. Further works as [52], [53] employed backpropagation-inspired approaches to find the optimal SIMs configurations for specific tasks like channel estimation, image reconstruction, or DoA estimation.

To illustrate, let us consider a SIM-based receiving antenna as depicted in Fig. 9, where a receiving SIM composed of L metasurface layers is followed by a conventional antenna array, such as an ULA, consisting of N_A active antennas, being N_A also the number of receiving RF chains. For simplicity, we assume that every metasurface layer composing the SIM is equipped with the same number M of meta-atoms, where $M \geq N_A$. Moreover, we assume that each layer of the SIM has an isomorphic square lattice arrangement and we model each metasurface layer as a uniform planar array [49]. Specifically, the distance between adjacent meta-atoms is denoted as d_{atom} , the area of each meta-atom is A , and the spacing between each metasurface layer is represented by d_{layer} .

The transmission coefficient of the m -th meta-atom in the l -th metasurface layer is represented

by $\phi_m^{(l)} = e^{j\theta_m^{(l)}}$, with $\theta_m^{(l)} \in [0, 2\pi)$, for $m = 1, 2, \dots, M$ and $l = 1, 2, \dots, L$. Consequently, the matrix of transmission coefficients for the l -th metasurface layer can be expressed as $\Phi^{(l)} = \text{diag}(\phi_1^{(l)}, \phi_2^{(l)}, \dots, \phi_M^{(l)}) \in \mathbb{C}^{M \times M}$. Moreover, we denote the intra-layer propagation matrix of the SIM, which describes the transmission coefficients from the $(l-1)$ -th transmit metasurface layer to the l -th layer, as $\mathbf{W}^{(l)} \in \mathbb{C}^{M \times M}$ for $l = 1, 2, \dots, L$. According to Rayleigh-Sommerfeld diffraction theory [35], the (m, i) -th entry of $\mathbf{W}^{(l)}$ is expressed as

$$w_{m,i}^{(l)} = \frac{A d_{\text{layer}}}{d_{m,i}^{(l)}} \left(\frac{1}{2\pi d_{m,i}^{(l)}} - \frac{j}{\lambda} \right) e^{jk_0 d_{m,i}^{(l)}}, \quad l = 1, 2, \dots, L \quad (42)$$

where $d_{m,i}^{(l)}$ is the transmission distance from the i -th meta-atom of the $(l-1)$ -th metasurface layer to the m -th meta-atom of the l -th layer. Therefore, the overall effect of the receiving SIM can be represented as

$$\mathbf{R}(\theta) = \Phi^{(L)} \mathbf{W}^{(L)} \dots \Phi^{(2)} \mathbf{W}^{(2)} \Phi^{(1)} \mathbf{W}^{(1)} \in \mathbb{C}^{M \times M}$$

where $\theta = \{\theta_m^{(l)}\}$, for $m = 1, 2, \dots, M$, $l = 1, 2, \dots, L$, collects all the parameters to be optimized. In addition, we assume that the receiving ULA is positioned close to the last SIM layer, that is, within its reactive near-field propagation region. Consequently, the wireless interaction between the receive ULA and the last layer of the SIM is characterized by the matrix $\mathbf{H}_R = \{h_{m,s}\} \in \mathbb{C}^{N_A \times M}$, whose elements can be derived by substituting $d_{m,i}^{(l)}$ in (42) with $r_{m,s}^{(1)}$, i.e., the distance between the m -th meta-atom of the last layer of the SIM and the generic s -th receiving antenna. Note that, despite matrices $\Phi^{(l)}$ are diagonal, the coupling effect at each layer makes the overall reflection matrix $\mathbf{R}(\theta)$ non-diagonal thus increasing the variables available for the optimization. When optimizing the phase profiles of the SIM for a given task, e.g., to realize an EM MIMO precoder, perform localization or channel estimation, the optimization problem that needs to be addressed is often a particular case of (40), which typically is in the form [33]

$$\underset{\theta}{\text{minimize}} \quad \Gamma = \|\mathbf{R}(\theta) \mathbf{H}_R - \mathbf{H}_0\|_F^2 \quad (43)$$

where \mathbf{H}_0 is a target response matrix that depends on the specific functionality to be achieved. Thanks to the layered structure of the SIM, the solution to (43) can be found thanks to a gradient descent algorithm based on error back-propagation, as outlined in Algorithm 1.

For instance, an interesting application of the algorithm mentioned above can be found in [53], where the Authors formulate an optimization problem in the form of (43) to compute the 2D DFT in the wave domain, hence propose a gradient descent algorithm to obtain a near-optimal solution for the SIM transmission coefficients, minimizing the Frobenius norm of the approximation error between the SIM's end-to-end transfer function and the ideal 2D DFT matrix \mathbf{H}_0 . The final objective of [53] is to leverage the 2D DFT, resulting from the propagation of the incident wave through the optimized SIM, to estimate the DoA of the signal at the receiving antenna array placed after the SIM.

Algorithm 1: Gradient Descent Algorithm for Solving (43)

-
- 1: **Input:** $\mathbf{W}^{(l)}$, $l = 1, \dots, L$, \mathbf{H}_0
 - 2: Randomly initialize the phase shifts $\theta_m^{(l)}$, $m = 1, \dots, M$, $l = 1, \dots, L$
 - 3: **repeat**
 - 4: Calculate the partial derivatives of Γ w.r.t. $\theta_m^{(l)}$, $m = 1, \dots, M$, $l = 1, \dots, L$
 - 5: Normalize the partial derivatives of Γ w.r.t. $\theta_m^{(l)}$, $m = 1, \dots, M$, $l = 1, \dots, L$
 - 6: Update the phase shifts $\theta_m^{(l)}$, $m = 1, \dots, M$, $l = 1, \dots, L$
 - 7: Diminish the learning rate η
 - 8: Calculate the objective function value Γ
 - 9: **until** The decrement of Γ is less than a preset threshold or the maximum number of iterations is reached
 - 10: **Output:** $\theta_m^{(l)}$, $m = 1, \dots, M$, $l = 1, \dots, L$
-

In the absence of noise, the EM waves propagating through the SIM are automatically focused on the specific receiving antenna corresponding to the on-grid DoA estimate of the incoming signal thanks to the 2D DFT operation. As a result, the DoA of the incoming signal can be readily estimated by simply measuring the energy distribution across the receiver antenna array.

In this regard, in Fig. 9-right the performance of such a DoA estimator is reported from [53], in comparison to the conventional method based on digital beamforming. Specifically, the mean squared error (MSE) of the electrical DoA angles ψ_x and ψ_y in the x- and y-directions is reported. The results show that the SIM-based estimator, operating with $N_A = 4 \times 4 = 16$ antennas and collecting the received signals over $T = 64$ snapshots before DoA estimation, performs comparably to the digital beamforming-based method with the same number of receiver antennas at large signal-to-noise ratios (SNRs). Additionally, Fig. 9-right plots the MSE of a 32×32 digital receiver array with a single snapshot, which provides a lower bound for the SIM-based scheme.

The results indicate that the SIM-based estimator performs comparably to the digital method, with the benefit of relying on energy detection and wave-based signal processing instead of coherent receivers and complex digital processing. Moreover, despite the superior accuracy, the reference digital approach demands a significantly larger array aperture with much more RF chains. In contrast, the SIM-based estimator achieves effective DoA estimation with a smaller array, demonstrating its practical advantage in resource-constrained scenarios. Details regarding the settings used to obtain the numerical results presented in Fig. 9 are available in [53].

Another interesting application can be found in [32], which introduces a novel microwave-based diffractive deep neural network (D^2NN) designed to classify handwritten metallic digits. The proposed

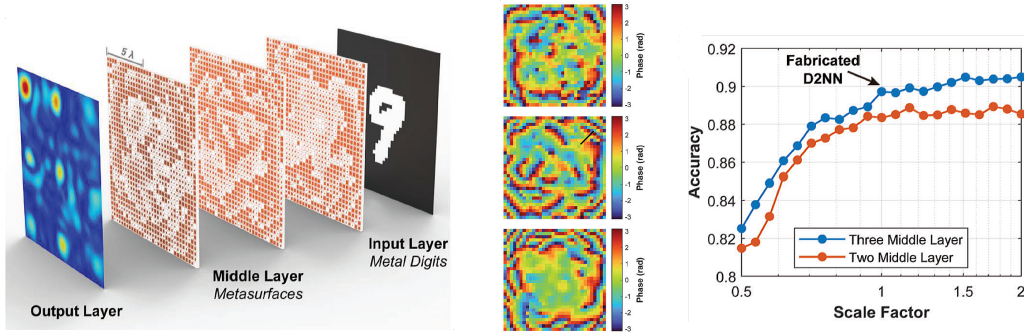


Fig. 10. Left: Workflow of the SIM-based D²NN. Center: Optimized phase distributions for the three metasurface layers. Right: Classification accuracy as a function of system scale and number of metasurface layers [32].

architecture consists of a SIM comprising $L = 3$ sequential metasurface layers, each of them having $M = 1024$ meta-atoms capable of introducing phase modulation to the impinging EM field. Input data, represented as engraved metal digit patterns, are illuminated by EM waves, propagating through the D²NN layers, and focusing energy at specific points on the target plane, hence enabling classification. The phase responses of each layer are designed using a stochastic gradient descent algorithm to minimize a cross-entropy loss function based on a training dataset. The system workflow is depicted in Fig. 10-left, which shows the overall SIM structure, including the input plane of engraved digits and the output layer with the EM field distribution which focuses the energy onto designated points at the target plane for direct classification. The optimized phase distributions of the three diffractive layers, presented in Fig. 10-middle, illustrate how the SIM processes input data by modulating the phase of the transmitted EM waves. These distributions reveal that the D²NN architecture progressively refine the wavefront, enabling precise focusing at the output plane and effectively mapping the input patterns into distinct classification categories. The phase patterns also highlight the network’s spatial symmetry and its ability to represent complex mappings within its design constraints. Finally, Fig. 10-right examines the classification accuracy as a function of the relative scale of the intermediate diffractive layers, i.e., based on the number of meta-atoms per layer side. The results indicate that the accuracy improves with increasing scale, plateauing at approximately 90.4% for a three-layer configuration, validating the efficiency of the gradient descent algorithm-based optimization in achieving high classification accuracy using a SIM.

C. EM Signal Processing in the Radiative Region

1) *Reconfigurable Intelligent Surfaces*: From a structural viewpoint, RISs are composed of large arrays comprising a multitude of small, programmable scattering elements that can dynamically control the phase and, in some cases, the amplitude of incident EM waves. By carefully configuring these

parameters, RISs can shape the wireless propagation environment, leading to significant improvements in coverage, capacity, and energy efficiency. Unlike conventional amplify-and-forward or relay nodes, which introduce transmission delays and consume significant power, RISs offer low implementation complexity and reduced power consumption, making them a highly attractive solution for various applications and to realize large structures. Moreover, RISs can be deployed in two main configurations: transmitting and reflecting. Transmitting RISs are designed to allow EM waves to pass through while adjusting their peculiar characteristics [54]. For instance, they can be used to control the propagation between indoor and outdoor environments or as layers in a SIM. Instead, reflecting RISs manipulate incoming EM waves by directing them via controlled reflections. In this section, we focus exclusively on the latter configuration.

Specifically, by applying specific phase shifts to the incident EM waves, RISs can reflect signals in directions that deviate from the conventional Snell's law. This phenomenon, referred to as the *universal Snell's law*, allows RISs to impose arbitrary directionality on reflected signals, resulting in highly customizable beamforming and beam focusing. This capability enhances signal strength and reception, and depending on the specific hardware structure and reconfigurable elements of the RIS, additional functionalities such as beam collimation, beam splitting, polarization control, and various forms of analog processing can also be achieved [22]–[25]. This versatility positions RISs as a promising solution for addressing the complex challenges faced in modern wireless communication systems. Applications of RISs span communication, sensing, localization/tracking, and the detection of passive objects. Ongoing research is also investigating new avenues for leveraging RISs in mapping and imaging to reconstruct high-fidelity and high-resolution maps of the surrounding radio environment [55].

As an example of the basic functionality of a RIS, let us consider a transmitting antenna, e.g., an access point (AP), that wants to transmit to a user equipment (UE) that is not in direct visibility due to obstruction raised by the presence of an obstacle, e.g., in a configuration similar to Fig. 11. Thanks to the deployment of the RIS, it is possible to create a virtual line-of-sight (LOS) link between the AP and the UE. Specifically, we consider a square RIS consisting of K small unit cells (i.e., scattering elements) spaced $\lambda/2$ apart providing reconfigurable phase shifts, each being characterized by reflection coefficients $\rho_{i,j} = e^{j\theta_{i,j}}$, with $i, j = 1, 2, \dots, \sqrt{K}$ being the 2D position indexes. According to the discussion in Sec. III-C, a conventional RIS with uncoupled elements is characterized by a diagonal reflection matrix $\mathbf{R}(\boldsymbol{\theta}) = \text{diag}(r_1, r_2, \dots, r_K)$ (diagonal RIS), where $r_k = \rho_{i,j}$ is the reflection coefficient of the k -th element at position (i, j) , where $k = i + \sqrt{K}(j - 1)$, with $i, j = 1, 2, \dots, \sqrt{K}$.

To perform the so-called *anomalous reflection*, i.e., let the RIS reflect the incoming EM wave at an arbitrary angle, the reflection coefficient applied at each RIS element must be configured such that

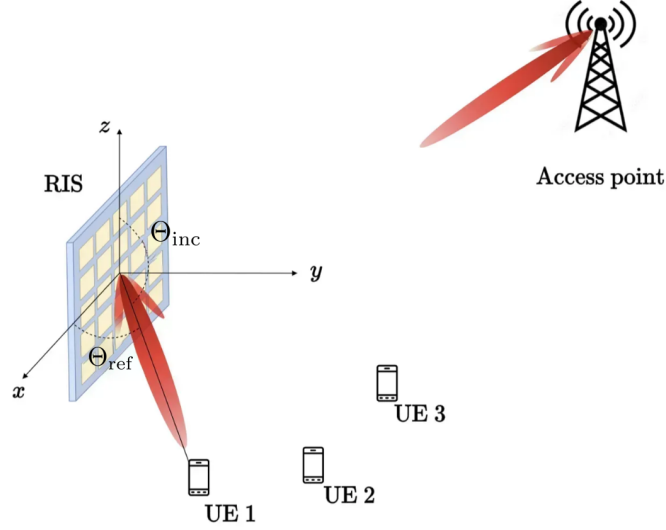


Fig. 11. RIS-aided LOS MIMO communication.

the phase shift introduced by the (i, j) -th element compensates the extra phase shifts due its position with respect to the incoming and reflected wavefronts, that is [23]

$$\theta_{i,j} = -\pi i (u_x(\Theta_{\text{inc}}) + u_x(\Theta_{\text{ref}})) - \pi j (u_y(\Theta_{\text{inc}}) + u_y(\Theta_{\text{ref}})) \quad (44)$$

where $\Theta_{\text{inc}} = (\theta_{\text{inc}}, \phi_{\text{inc}})$ represents the incident angle (evaluated with respect to the RIS's normal vector), $\Theta_{\text{ref}} = (\theta_{\text{ref}}, \phi_{\text{ref}})$ represents the desired reflection angle, $u_x(\Theta)$ and $u_y(\Theta)$ are functions of the elevation (θ) and azimuth (ϕ) angles, i.e., $u_x(\Theta) = \sin(\theta) \cos(\phi)$ and $u_y(\Theta) = \sin(\theta) \sin(\phi)$. In this manner, the RIS can steer the reflected signal towards a specific angle, enabling a high degree of control over the propagation of the EM waves.

One important issue, often overlooked in the literature, arises from reflections in unwanted directions caused by uncontrolled RF sources in the environment. These reflections can generate interference, which may be challenging to mitigate. Diagonal RISs may be ineffective in addressing this problem due to the limited available number of DoF in their reflection matrix, which is equal to K . A potential alternative is the use of non-diagonal RISs, which allow controllable coupling between elements. This configuration significantly increases the available number of DoF, reaching up to $K(K-1)/2$ in reciprocal structures [45]. An even greater number of DoF (up to K^2) can be achieved with non-reciprocal designs. Interestingly, a non-diagonal RIS, as a 2D structure, could theoretically achieve the same performance as a SIM, which is a 3D structure but with 2D input and output surfaces. However, as both technologies are still in their early stages, a detailed comparison in terms of implementation complexity is not yet available.

2) *Self-Conjugating Metasurfaces*: We now present an example of iterative over-the-air EM processing involving two devices located within their respective radiative regions. The objective is to

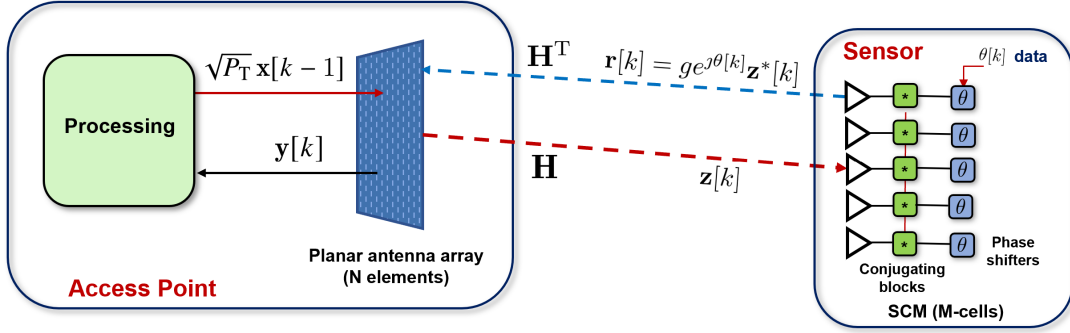


Fig. 12. Principle scheme of a modulating SCM-based MIMO communication.

achieve joint communication and optimal beamforming in a MIMO link without requiring channel state information (CSI) estimation or signaling, thereby reducing the latency and overhead typically associated with large MIMO systems. The idea is to exploit an EM device at one end of the link that performs the complex conjugation of the signal coming from the other device, thereby achieving retrodirectivity. Due to this processing capability, such a device is referred to as self-conjugating metasurface (SCM). Additionally, it is envisioned that the SCM introduces appropriate phase shifts, uniformly across all cells, into the retransmitted signals, thereby incorporating information through phase modulation,

This dual-function device, referred to as a *modulating SCM* in the following, can be considered an evolution of retrodirective antenna arrays, which are systems capable of reflecting incoming signals back toward their direction of arrival [56]. While retrodirective antennas have been studied for decades, the feasibility of retrodirective metasurfaces has only recently been demonstrated in the literature [57]. By leveraging *modulating* SCMs, it is possible to devise a communication scheme that involves an iterative exchange of signals between a full-duplex central unit equipped with a conventional antenna array with N elements, such as an AP, and a device equipped with a *modulating* SCM with M elements, such as a sensor, which has queued data intended for the AP. The former continuously transmits an interrogation signal while the latter retro-directs the received signal after modulating it according to the data addressed to the interrogation device.

An algorithm designed to establish such an uplink MIMO communication with joint beamforming and data transmission, proposed in [17], is presented in pseudo-code form in Algorithm 2 and is discussed below. The key quantities referenced in Algorithm 2 are highlighted in Fig. 12.

The process begins (step 0 of the pseudo-code) with the AP generating a beamforming vector, $\mathbf{x}[0] \in \mathbb{C}^{1 \times N}$. Since the position of the sensor is unknown at startup, this initial beamforming vector is chosen randomly (with norm one) to allow the signal transmitted using $\mathbf{x}[0]$ to cover multiple directions, as shown in Fig. 13, first beam pattern. Obviously, any prior information (e.g., past transmission, the

Algorithm 2: Modified *Power Method* for joint communication and beamforming between sensor - AP

```

0: Initialization: generate a guess unit norm beamforming vector  $\mathbf{x}[0]$  ;
1: for  $k = 1, \dots, K$  do
    2: transmit:  $\sqrt{P_T} \mathbf{x}[k-1]$  ; // signal transmitted by the AP
    3:  $\mathbf{z}[k] = \sqrt{P_T} \mathbf{H} \mathbf{x}[k-1] + \boldsymbol{\eta}[k]$  ; // signal received by the sensor
    4:  $\mathbf{r}[k] = g e^{j\theta[k]} \mathbf{z}^*[k]$  ; // signal retro-directed by the sensor
    5: receive:  $\mathbf{y}[k] = e^{j\theta[k]} \mathbf{A}^* \mathbf{x}^*[k-1] + \mathbf{n}^*[k]$  ; // signal received by the AP
    6:  $\mathbf{x}[k] = \mathbf{y}^*[k] / \|\mathbf{y}[k]\|$  ; // beamforming vector update
    7:  $u[k] = \mathbf{x}^H[k-1] \mathbf{x}[k]$  ; // decision variable
    8:  $\hat{\theta}[k] = \text{detection}(-\arg\{u[k]\})$  ; // data detection
end

```

position of the sensor, etc.) can be exploited to speed up the estimation of the optimal beamforming vector. An iterative process is then initiated (see Algorithm 2) to progressively steer the downlink beam toward the active sensor based on the signal it has retro-directed. More precisely, at the $(k-1)$ -th iteration, with $k \geq 1$, the AP transmits the interrogation signal with power P_T using the current beamforming vector $\mathbf{x}[k-1]$ (step 2).

This signal, after passing through the MIMO channel represented by the matrix $\mathbf{H} \in \mathbb{C}^{M \times N}$, is then received by the sensor (step 3), along with the AWGN noise $\boldsymbol{\eta}[k] \in \mathbb{C}^{1 \times M}$. Thanks to the *modulating* SCM, the sensor reflects the received signal along the direction(s) of arrival, also changing its phase based on the data intended for the AP (step 4). Specifically, at the sensor side, information data is associated with the phase sequence $\{\theta[k]\}_{k=1}^K$, forming a packet of length K symbols, according to any phase-based signaling scheme (e.g., BPSK). When reflecting the signal, the *modulating* SCM may also introduce a gain g , with $g < 1$ if it is passive. In step 5, the AP receives the response $\mathbf{y}[k] \in \mathbb{C}^{1 \times N}$ from the sensor, which incorporates the total AWGN at the receiver, $\mathbf{n}[k] \in \mathbb{C}^{1 \times N}$, and accounts for the round-trip path experienced by the signal and the conjugation performed by the SCM through the matrix $\mathbf{A} = \sqrt{P_T} g \mathbf{H}^H \mathbf{H} \in \mathbb{C}^{N \times N}$. Then, a normalized and conjugated version of the received vector $\mathbf{y}[k]$ is computed (step 6) and used as the updated beamforming vector $\mathbf{x}[k]$ in the subsequent iteration (see Fig. 13, second beam pattern).

Iteration after iteration, the beamforming vector is progressively refined over the air, ideally converging toward the optimal configuration (see Fig. 13, third beam pattern). Information data is also extracted by the AP at each iteration by correlating the current received vector with the previous beamforming vector $\mathbf{x}^H[k-1]$, thus forming the scalar decision variable $u[k]$ (step 7). The decision

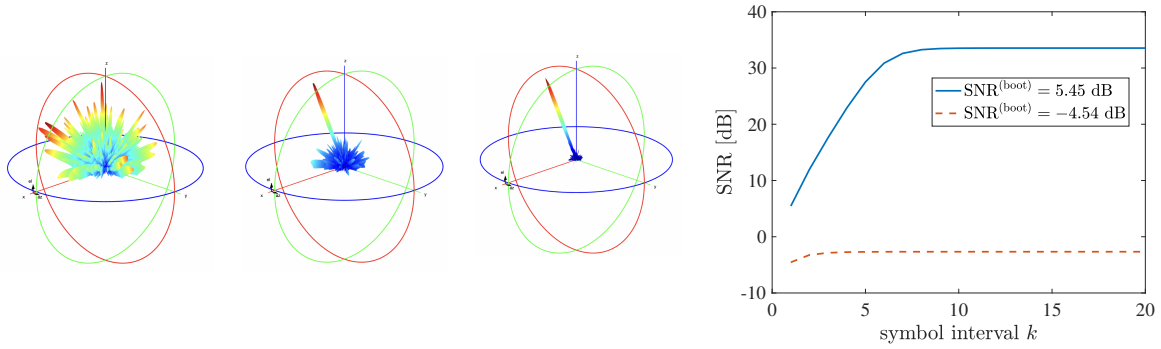


Fig. 13. Evolution of the beam's shape at time $k = 0$, $k = 1$, and $k = 2$, and evolution of the SNR for different bootstrap conditions in the case of rank-1 channel.

on the modulation symbol conveyed by $\hat{\theta}[k]$ at the k -th time instant is obtained by means of the function $\text{detection}(\cdot)$, according to the adopted modulation scheme (step 8). It is worth noting that data demodulation occurs while the AP transmits the interrogation signal using the current beamforming vector, thanks to the full-duplex capability of the AP.

In the absence of noise and data, the processing operated in Algorithm 2 corresponds to the well-known *Power Method*, which allows the estimate of the strongest eigenvector (top eigenvector) of a square matrix \mathbf{A} , described by the recurrence relation

$$\mathbf{x}[k] = \frac{\mathbf{A} \mathbf{x}[k-1]}{\|\mathbf{A} \mathbf{x}[k-1]\|} \quad (45)$$

being $\mathbf{x}[0]$ typically an initial random guess of the top eigenvector. For $k \rightarrow \infty$, the direction of $\mathbf{x}[k]$ converges to that of the top eigenvector. This means that $\mathbf{x}[k]$ tends to the direction of the top left eigenvector of the MIMO channel matrix \mathbf{H} , i.e., the optimal beamforming vector. In the presence of noise, new noise samples enter the loop at each iteration, and the convergence to the top eigenvector of the channel is no longer guaranteed. In this regard, the analysis in [17] shows that the iterative scheme still converges to the top eigenvector if the *bootstrap* SNR, defined as $\text{SNR}^{(\text{boot})} = \text{SNR}^{(\text{max})}/N$, is greater than one, where $\text{SNR}^{(\text{max})}$ denotes the maximum SNR achievable along the direction of the top eigenvector, which occurs when the AP beam is perfectly aligned with the sensor. When the algorithm operates successfully, the SNR experienced by the AP at the k -th iteration, denoted $\text{SNR}[k]$, converges iteratively to $\text{SNR}^{(\text{max})}$ independently of the initial guess $\mathbf{x}[0]$.

In Fig. 13, we also report some simulation results to investigate the performance of the scheme proposed in [17]. The scenario considered consists of an AP operating at 28 GHz and equipped with a uniform planar array of $N = 20 \times 20$ antennas deployed along the xy -plane and a sensor with a *modulating* SCM comprising $M = 10 \times 10$ cells assumed to lie on the same plane. Specifically, Fig. 13 shows the time evolution of $\text{SNR}[k]$ under different conditions: The blue curve corresponds

to the case $\text{SNR}^{(\max)} = 35$ dB, associated with a *bootstrap* SNR of 5.45 dB, while the red curve corresponds to the case $\text{SNR}^{(\max)} = 25$ dB, resulting in a *bootstrap* SNR of -5.45 dB. As shown, when $\text{SNR}^{(\text{boot})}$ exceeds 0 dB, $\text{SNR}[k]$ converges to $\text{SNR}^{(\max)}$ after a few iterations, indicating that perfect alignment has been achieved and the packet can be successfully detected. Conversely, when $\text{SNR}^{(\text{boot})}$ is below 0 dB, $\text{SNR}[k]$ converges to a much lower value and the link cannot be established.

It is worth noticing that the convergence time is below 10 time intervals, as confirmed by a more extensive investigation available in [17]. The algorithm is able to dynamically adjust the beam orientation in response to any change in the position of the sensor during ongoing communication, thereby exhibiting tracking capabilities. Notably, this is achieved without requiring analog-to-digital converter (ADC) chains at the UE, explicit channel estimation, and time-consuming beamforming or alignment processes. Application of this solution to grant-free random access schemes can be found in [58].

VI. DISCUSSION AND FUTURE RESEARCH DIRECTIONS

In the previous sections, we explored the significant advancements in the development of ESP in recent years. By processing the signal directly at the EM level through the interaction of passive scatterers, ESP offers considerable benefits, including reduced power consumption, lower latency, and smaller device size compared to fully digital or hybrid alternatives. These features make ESP-based solutions highly promising for addressing scalability and sustainability challenges. However, these advantages are accompanied by trade-offs. New challenges must be considered, as they may limit the processing flexibility and applicability of these solutions compared to traditional digital-based implementations. Specifically, signal processing schemes must account for constraints imposed by fundamental EM laws, and the characteristics of the specific technology employed can further restrict the DoF available for implementing certain functionalities, as demonstrated in the previous sections. Therefore, it is crucial to adopt physically consistent models and design tailored EM-compliant signal processing methods.

Despite the recent progress discussed in this article, significant work remains to be done to address various issues at the intersection of EM and signal processing theory. Here, we highlight some promising research directions:

- *Optimization algorithms*: From the SP perspective, the primary challenges lie in developing efficient techniques to address high-dimensional optimization problems constrained by EM laws, such as that expressed in (40), particularly when dealing with a large number of reconfigurable scattering elements. To achieve an improved balance between power consumption, scalability, latency, and processing flexibility, hybrid schemes that jointly optimize the digital and EM

sections can also be explored. Another open challenge involves designing optimization techniques capable of determining the optimal geometric configuration of scatterers to achieve a desired class of signal processing functionalities.

- *Space-time-frequency EM processing*: Most of the existing literature has focused on linear, time-invariant ESP solutions that operate primarily in the spatial domain. Consequently, our analysis in the previous sections has been largely confined to narrowband and time-invariant systems. However, emerging research is exploring the extension of these concepts to wideband and time-varying systems, addressing processing across the space, time, and frequency domains. For instance, EM devices operating with wideband signals often exhibit frequency-dependent effects, such as beam squinting or unwanted phase variations. While traditionally viewed as limitations, these phenomena can be strategically harnessed to enhance EM-level functionalities. By deliberately exploiting frequency-dependent behaviors, it becomes possible to design systems capable of tailored responses for signals at different frequencies. This approach is particularly relevant in the study of space-time modulated (STM)-RIS, also known as space-time modulated metasurfaces (STMM), which integrate phase and temporal phase gradients across metasurfaces to enable anomalous, non-reciprocal reflections [59]. This working principle generalizes the design concepts of traditional RIS.

Another promising research direction involves integrating these concepts with optical technologies, potentially combining the strengths of both domains to unlock new capabilities.

- *CSI estimation*: The examples of scattering device optimization presented in the previous sections implicitly assume the availability of a perfect CSI estimate or precise knowledge of the geometry, including the position and orientation of devices. However, in some scenarios, the scattering device may be located far from the active system components (e.g., a RIS) and lack integrated sensors. In dynamic environments, estimating the cascade channel can become time-consuming, leading to high latency and overhead. Potential solutions could involve long-term statistical optimization schemes that leverage statistical priors, such as device positioning uncertainty and behavioral patterns [60].
- *Artificial intelligence (AI)-aided ESP and ESP-aided AI*: To address the so-called curse of dimensionality in reconfigurable scatterer optimization, AI-aided schemes that incorporate physically consistent models can be employed. Additionally, AI-based methods can be leveraged to develop hybrid solutions, where AI-driven optimization techniques are combined with traditional model-based approaches. This integration can lead to the creation of more efficient and adaptive ESP systems, capable of handling complex and dynamic signal processing tasks. Conversely, non-linear elements can be incorporated into reconfigurable scattering devices, such as SIMs, to emulate the behavior of a DNN through the EM device. However, unlike conventional DNNs,

where weights and activation functions can be freely chosen, EM physical and technological constraints impose additional limitations. Consequently, models and training schemes must be reimaged to accommodate these constraints.

In summary, while existing research has offered invaluable insights into the practical and theoretical aspects of EM signal processing, there is still much to explore. Advancing this field will require the seamless integration of cutting-edge technologies, such as AI and innovative materials, with established physical principles from electromagnetism and related disciplines. This synergy will be pivotal in driving the next wave of innovation and positioning ESP as a key enabler for future wireless networks.

ACKNOWLEDGMENT

This work was supported by the European Union under the Italian National Recovery and Resilience Plan (NRRP) of NextGeneration EU, partnership on “Telecommunications of the Future” (PE00000001 - program “RESTART”), and by the HORIZON-JU-SNS-2022-STREAM-B-01-03 6G-SHINE project (Grant Agreement No. 101095738). Giulia Torcolacci was funded by an NRRP Ph.D. grant.

REFERENCES

- [1] P. L. McMahon, “The physics of optical computing,” *Nature Reviews Physics*, vol. 5, p. 717–734, 2023.
- [2] M. Alsabah *et al.*, “6G wireless communications networks: A comprehensive survey,” *IEEE Access*, vol. 9, pp. 148 191–148 243, Nov. 2021.
- [3] N. González-Prelcic *et al.*, “The integrated sensing and communication revolution for 6G: Vision, techniques, and applications,” *Proc. IEEE*, vol. 112, no. 7, pp. 1–16, Jul. 2024.
- [4] E. Björnson, Y. C. Eldar, E. G. Larsson, A. Lozano, and H. V. Poor, “Twenty-five years of signal processing advances for multiantenna communications: From theory to mainstream technology,” *IEEE Signal Proc. Mag.*, vol. 40, no. 4, pp. 107–117, Jun. 2023.
- [5] D. Dardari, “Communicating with large intelligent surfaces: Fundamental limits and models,” *IEEE J. Select. Areas Commun.*, vol. 38, no. 11, pp. 2526–2537, Nov. 2020.
- [6] C. You, Y. Cai, Y. Liu, M. Di Renzo, T. M. Duman, A. Yener, and A. L. Swindlehurst, “Next Generation Advanced Transceiver Technologies for 6G,” *arXiv e-prints*, p. arXiv:2403.16458, Mar. 2024.
- [7] H. Zhang, N. Shlezinger, F. Guidi, D. Dardari, and Y. C. Eldar, “6G wireless communications: From far-field beam steering to near-field beam focusing,” *IEEE Commun. Mag.*, vol. 61, no. 4, pp. 72–77, Apr. 2023.
- [8] D. Dardari and N. Decarli, “Holographic communication using intelligent surfaces,” *IEEE Commun. Mag.*, vol. 59, no. 6, pp. 35–41, Jun. 2021.
- [9] J. Zhu, Z. Wan, L. Dai, M. Debbah, and H. V. Poor, “Electromagnetic information theory: Fundamentals, modeling, applications, and open problems,” *IEEE Wireless Commun. Mag.*, vol. 31, no. 3, pp. 156–162, Jun. 2024.
- [10] M. D. Renzo and M. D. Migliore, “Electromagnetic signal and information theory,” *IEEE BITS the Information Theory Magazine*, pp. 1–13, 2024.
- [11] E. Björnson *et al.*, “Towards 6G MIMO: Massive spatial multiplexing, dense arrays, and interplay between electromagnetics and processing,” *arXiv e-prints*, p. arXiv:2401.02844, Jan. 2024.

- [12] L. Wei *et al.*, “Electromagnetic information theory for holographic MIMO communications,” *arXiv e-prints*, p. arXiv:2405.10496, May 2024.
- [13] M. D. Migliore, “Who cares about the horse? A gentle introduction to information in electromagnetic theory,” *IEEE Antennas Propag. Mag.*, vol. 62, no. 5, pp. 126–137, Oct. 2020.
- [14] C. Caloz, S. Gupta, Q. Zhang, and B. Nikfal, “Analog signal processing: A possible alternative or complement to dominantly digital radio schemes,” *IEEE Microw. Mag.*, vol. 14, no. 6, pp. 87–103, Sep. 2013.
- [15] D. Dardari, “Reconfigurable electromagnetic environments: A general framework,” *IEEE J. Select. Areas Commun.*, vol. 42, no. 6, pp. 1479–1493, Jun. 2024.
- [16] Y.-C. Liang, Q. Zhang, J. Wang, R. Long, H. Zhou, and G. Yang, “Backscatter communication assisted by reconfigurable intelligent surfaces,” *Proc. IEEE*, vol. 110, no. 9, pp. 1339–1357, Sep. 2022.
- [17] D. Dardari, M. Lotti, N. Decarli, and G. Pasolini, “Establishing multi-user MIMO communications automatically using retrodirective arrays,” *IEEE Open J. Commun. Soc.*, vol. 4, pp. 1396–1416, Jun. 2023.
- [18] L. Zhang *et al.*, “Space-time-coding digital metasurfaces,” *Nature Communications*, vol. 9, no. 1, p. 4334, Oct 2018.
- [19] J. Mautz and R. Harrington, “Modal analysis of loaded N-port scatterers,” *IEEE Trans. Antennas Propagat.*, vol. 21, no. 2, pp. 188–199, Mar. 1973.
- [20] R. Harrington, “Reactively controlled directive arrays,” *IEEE Trans. Antennas Propag.*, vol. 26, no. 3, pp. 390–395, May 1978.
- [21] M. Barbuto, Z. Hamzavi-Zarghani, M. Longhi, A. Monti, D. Ramaccia, S. Vellucci, A. Toscano, and F. Bilotti, “Metasurfaces 3.0: a new paradigm for enabling smart electromagnetic environments,” *IEEE Trans. Antennas Propagat.*, vol. 70, no. 10, pp. 8883 – 8897, Oct. 2021.
- [22] E. Martini and S. Maci, “Theory, analysis, and design of metasurfaces for smart radio environments,” *Proc. IEEE*, vol. 110, no. 9, pp. 1227–1243, Sep. 2022.
- [23] M. Di Renzo, A. Zappone, M. Debbah, M.-S. Alouini, C. Yuen, J. de Rosny, and S. Tretyakov, “Smart radio environments empowered by reconfigurable intelligent surfaces: How it works, state of research, and the road ahead,” *IEEE J. Select. Areas Commun.*, vol. 38, no. 11, pp. 2450–2525, Nov. 2020.
- [24] M. Di Renzo, F. H. Danufane, and S. Tretyakov, “Communication models for reconfigurable intelligent surfaces: From surface electromagnetics to wireless networks optimization,” *Proc. IEEE*, vol. 110, no. 9, pp. 1164–1209, Sep. 2022.
- [25] E. Björnson, H. Wymeersch, B. Matthiesen, P. Popovski, L. Sanguinetti, and E. de Carvalho, “Reconfigurable intelligent surfaces: A signal processing perspective with wireless applications,” *IEEE Signal Processing Mag.*, vol. 39, no. 2, pp. 135–158, Mar. 2022.
- [26] Z. Wang, J. Zhang, H. Du, W. E. I. Sha, B. Ai, D. Niyato, and M. Debbah, “Extremely large-scale MIMO: Fundamentals, challenges, solutions, and future directions,” *IEEE Wireless Commun.*, vol. 31, no. 3, pp. 1–9, Jun. 2023.
- [27] T. Gong *et al.*, “Holographic MIMO communications: Theoretical foundations, enabling technologies, and future directions,” *IEEE Commun. Surveys & Tutorials*, vol. 26, no. 1, pp. 196–257, 2024.
- [28] K.-K. Wong, W. K. New, X. Hao, K.-F. Tong, and C.-B. Chae, “Fluid antenna system - Part I: Preliminaries,” *IEEE Commun. Lett.*, vol. 27, no. 8, pp. 1919–1923, Aug. 2023.
- [29] J. C. Bucheli Garcia, M. Kamoun, and A. Sibille, “Low-complexity adaptive spatial processing of ESPAR antenna systems,” *IEEE Trans. Wireless Commun.*, vol. 19, no. 6, pp. 3700–3711, Feb. 2020.
- [30] D. Dardari, “3D electromagnetic signal processing,” in *Proc. Asilomar Conf. on Signals, Systems and Computers*, Oct 2024.
- [31] X. Lin, Y. Rivenson, N. T. Yardimci, M. Veli, Y. Luo, M. Jarrahi, and A. Ozcan, “All-optical machine learning using diffractive deep neural networks,” *Science*, vol. 361, no. 6406, pp. 1004–1008, 2018. [Online]. Available: <https://www.science.org/doi/abs/10.1126/science.aat8084>

- [32] Z. Gu, Q. Ma, X. Gao, J. W. You, and T. J. Cui, "Classification of metal handwritten digits based on microwave diffractive deep neural network," *Advanced Optical Materials*, vol. 12, no. 7, p. 2301938, 2024.
- [33] J. An, C. Xu, D. W. K. Ng, G. C. Alexandropoulos, C. Huang, C. Yuen, and L. Hanzo, "Stacked intelligent metasurfaces for efficient holographic MIMO communications in 6G," *IEEE J. Select. Areas Commun.*, vol. 41, no. 8, pp. 2380–2396, Aug. 2023.
- [34] A. Silva, F. Monticone, G. Castaldi, V. Galdi, A. Alù, and N. Engheta, "Performing mathematical operations with metamaterials," *Science*, vol. 343, no. 6167, pp. 160–163, 2014. [Online]. Available: <https://science.sciencemag.org/content/343/6167/160>
- [35] C. A. Balanis, *Antenna Theory: Analysis and Design*. New Jersey, USA: Wiley, 2016.
- [36] T. L. Marzetta, "Spatially-stationary propagating random field model for massive MIMO small-scale fading," in *2018 IEEE International Symposium on Information Theory (ISIT)*, 2018, pp. 391–395.
- [37] C. A. Balanis, *Advanced Engineering Electromagnetics*. Wiley, 2024.
- [38] M. Franceschetti, *Wave Theory of Information*. Cambridge, UK: Cambridge University press, 2018.
- [39] D. A. B. Miller, "Waves, modes, communications, and optics: A tutorial," *Adv. Opt. Photon.*, vol. 11, no. 3, pp. 679–825, Sep 2019. [Online]. Available: <http://aop.osa.org/abstract.cfm?URI=aop-11-3-679>
- [40] O. M. Bucci and T. Isernia, "Electromagnetic inverse scattering: Retrievable information and measurement strategies," *Radio Science*, vol. 32, no. 6, pp. 2123–2137, 1997.
- [41] A. Pizzo, A. d. J. Torres, L. Sanguinetti, and T. L. Marzetta, "Nyquist sampling and degrees of freedom of electromagnetic fields," *IEEE Trans. Signal Processing*, vol. 70, pp. 3935–3947, Jun. 2022.
- [42] D. Tse and P. Viswanath, *Fundamentals of Wireless Communication*. New York, NY: Cambridge University Press, 2005.
- [43] N. Decarli and D. Dardari, "Communication modes with large intelligent surfaces in the near field," *IEEE Access*, vol. 9, pp. 165 648–165 666, 2021.
- [44] G. Bartoli, A. Abrardo, N. Decarli, D. Dardari, and M. Di Renzo, "Spatial multiplexing in near field MIMO channels with reconfigurable intelligent surfaces," *IET Signal Processing*, vol. 17, no. 3, p. e12195, 2023. [Online]. Available: <https://ietresearch.onlinelibrary.wiley.com/doi/abs/10.1049/sil2.12195>
- [45] H. Li, S. Shen, M. Nerini, and B. Clerckx, "Reconfigurable intelligent surfaces 2.0: Beyond diagonal phase shift matrices," *IEEE Communications Magazine*, vol. 62, no. 3, pp. 102–108, 2024.
- [46] Z. Han, Y. Zhang, S. Shen, Y. Li, C.-Y. Chiu, and R. Murch, "Characteristic mode analysis of ESPAR for single-RF MIMO systems," *IEEE Trans. Wireless Commun.*, vol. 20, no. 4, pp. 2353–2367, Apr. 2021.
- [47] N. U. Hassan, J. An, M. Di Renzo, M. Debbah, and C. Yuen, "Efficient beamforming and radiation pattern control using stacked intelligent metasurfaces," *IEEE Open J. Commun. Soc.*, Jan. 2024.
- [48] V. Jamali, A. M. Tulino, G. Fischer, R. R. Müller, and R. Schober, "Intelligent surface-aided transmitter architectures for millimeter-wave ultra massive MIMO systems," *IEEE Open J. Commun. Soc.*, vol. 2, pp. 144–167, Dec. 2020.
- [49] C. Liu *et al.*, "A programmable diffractive deep neural network based on a digital-coding metasurface array," *Nature Electronics*, vol. 5, no. 2, pp. 113–122, Feb. 2022.
- [50] N. Stefan Perović and L.-N. Tran, "Mutual information optimization for SIM-based holographic MIMO systems," *IEEE Commun. Lett.*, vol. 28, no. 11, pp. 2583–2587, Nov. 2024.
- [51] A. Papazafeiropoulos, J. An, P. Kourtessis, T. Ratnarajah, and S. Chatzinotas, "Achievable rate optimization for stacked intelligent metasurface-assisted holographic MIMO communications," *IEEE Trans. Wireless Commun.*, vol. 23, Oct. 2024.
- [52] J. Li *et al.*, "Spectrally encoded single-pixel machine vision using diffractive networks," *Sci. Adv.*, vol. 7, no. 13, p. eabd7690, Mar. 2021.

- [53] J. An, C. Yuen, Y. L. Guan, M. Di Renzo, M. Debbah, H. V. Poor, and L. Hanzo, “Two-dimensional direction-of-arrival estimation using stacked intelligent metasurfaces,” *IEEE J. Select. Areas Commun.*, vol. 42, no. 10, Oct. 2024.
- [54] D. Demmer, F. Foglia Manzillo, S. Gharbieh, M. Śmierzchalski, R. D’Errico, J.-B. Doré, and A. Clemente, “Hybrid precoding applied to multi-beam transmitting reconfigurable intelligent surfaces (T-RIS),” *Electronics*, vol. 12, no. 5, p. 1162, Feb. 2023.
- [55] G. Torcolacci, A. Guerra, H. Zhang, F. Guidi, Q. Yang, Y. C. Eldar, and D. Dardari, “Holographic imaging with XL-MIMO and RIS: Illumination and reflection design,” *IEEE J. Sel. Topics Signal Processing*, vol. 18, no. 4, pp. 587–602, May 2024.
- [56] R. Miyamoto and T. Itoh, “Retrodirective arrays for wireless communications,” *IEEE Microwave Magazine*, vol. 3, no. 1, pp. 71–79, Mar. 2002.
- [57] M. Kalaagi and D. Seetharamdoo, “Multiangle retrodirective cascaded metasurface,” *Journal of Applied Physics*, vol. 126, no. 10, 09 2019, 104901. [Online]. Available: <https://doi.org/10.1063/1.5095147>
- [58] D. Dardari, M. Lotti, N. Decarli, and G. Pasolini, “Grant-free random access with backscattering self-conjugating metasurfaces,” *IEEE Trans. Cognitive Commun. Networking*, vol. 10, no. 5, pp. 1620–1634, Oct. 2024.
- [59] M. Mizmizi, D. Tagliaferri, and U. Spagnolini, “Wireless communications with space-time modulated metasurfaces,” *IEEE J. Select. Areas Commun.*, vol. 42, no. 6, pp. 1534–1548, Jun. 2024.
- [60] F. Jiang, A. Abrardo, K. Keykhosravi, H. Wymeersch, D. Dardari, and M. Di Renzo, “Two-timescale transmission design and RIS optimization for integrated localization and communications,” *IEEE Trans. Wireless Commun.*, vol. 22, no. 12, pp. 8587–8602, Dec. 2023.